

# A nearby He-rich superluminous supernova at photospheric phases

A. Fiore<sup>1,2\*</sup>, A. Kozyreva<sup>3</sup>, L. Yan<sup>4</sup>, S. Benetti<sup>2</sup>, J. P. Anderson<sup>5</sup>, P. Baklanov<sup>6,7,8</sup>, Y. -Z. Cai<sup>9,10</sup>, E. Cappellaro<sup>2</sup>, T.-W. Chen<sup>11</sup>, N. Elias-Rosa<sup>2,12</sup>, A. Gal-Yam<sup>13</sup>, M. J. Graham<sup>14</sup>, M. Gromadzki<sup>15</sup>, S. L. Groom<sup>16</sup>, C. P. Gutiérrez<sup>17,12</sup>, D. Hiramatsu<sup>18,19,20</sup>, D. A. Howell<sup>21,22</sup>, C. Inserra<sup>23</sup>, M. M. Kasliwal<sup>14</sup>, R. Könyves-Tóth<sup>24,25</sup>, P. Lundqvist<sup>26</sup>, C. McCully<sup>22</sup>, A. Mironov<sup>8</sup>, S. Moran<sup>27</sup>, T. E. Müller-Bravo<sup>28,29</sup>, M. Newsome<sup>30</sup>, M. Nicholl<sup>31</sup>, P. Ochner<sup>2,32</sup>, E. Padilla Gonzalez<sup>33</sup>, A. Pastorello<sup>2</sup>, P. J. Pessi<sup>26</sup>, G. Pignata<sup>34</sup>, F. Ragosta<sup>35,36</sup>, A. Reguitti<sup>2,37</sup>, T. M. Reynolds<sup>38,39,40</sup>, R. L. Riddle<sup>4</sup>, B. Rusholme<sup>16</sup>, I. Salmaso<sup>36,2</sup>, S. Schulze<sup>41</sup>, J. Sollerman<sup>26</sup>, L. Tomasella<sup>2</sup>, D. Warshofsky<sup>42</sup>, S. Yang<sup>43</sup>, and D. R. Young<sup>31</sup>

(Affiliations can be found after the references)

Received September 15, 20XX; accepted March 16, 20XX

## ABSTRACT

**Aims.** We present and interpret the data of the nearby hydrogen-deficient but helium-rich superluminous supernova SN 2021bnw which reached a magnitude of  $-20.7$  at maximum luminosity in  $g$  band.

**Methods.** We discuss the light curves and spectra of SN 2021bnw based on its spectro-photometric follow up exploiting different observational facilities. We reproduce the NIR spectrum of SN 2021bnw with TARDIS to inspect the chemical composition at late photospheric phases and identify helium features. We also use a STELLA model coupling hydrodynamics and radiation transport to constrain the physical parameters of the explosion assuming a  $^{56}\text{Ni}$ +CSM scenario.

**Results.** We suggest that SN 2021bnw was mainly powered by the interaction of the ejecta with a previously lost He-rich circumstellar material, coupled with a central power source.

**Conclusions.** This work expands the data sample of He-rich superluminous supernovae rich (SLSNe Ib) and, assuming a single progenitor scenario, can constrain the masses and the physics of their progenitors.

**Key words.** supernovae: individual

## 1. Introduction

At the end of their life, massive stars ( $\gtrsim 8 \text{ M}_\odot$ , e.g., Smartt 2009) undergo the gravitational collapse of their core and their outer layers can be ejected in a catastrophic fashion. This event may be accompanied by a luminous supernova (SN) whose luminosity is usually comprised between  $-14$  mag and  $-19$  at maximum in optical bands. A common explanation for the luminosity of stripped-envelope SNe (Taddia et al. 2018) considers the radioactive decay of  $\lesssim 0.1 - 0.3 \text{ M}_\odot$  of  $^{56}\text{Ni}$  (e.g., Anderson 2019). In the last two decades, observations of superluminous supernovae (SLSNe, usually brighter than  $\approx -20$  mag in the optical bands at maximum, Gal-Yam 2019) questioned this scenario. In fact, synthesizing more  $^{56}\text{Ni}$  is challenging for the classical neutrino-driven core-collapse paradigm (see e.g. Ugliano et al. 2012; Pejcha & Thompson 2015; Sukhbold et al. 2016; Terreran et al. 2017; Suwa et al. 2019, but see also Umeda & Nomoto 2008 for higher estimates of the  $^{56}\text{Ni}$  yield). There is still no consensus about the physics ruling SLSNe. The contribution of the spindown radiation from a newly born and rapidly spinning neutron star (e.g., Woosley 2010; Kasen & Bildsten 2010) and/or that of the interaction of the SN ejecta with a previously ejected circumstellar material (CSM, Chevalier & Fransson 2003) are viable explanations for interpreting SLSNe. Upon making reasonable assumptions to account for the lack of multi-component features in the spectra of SLSNe I (see e.g., Smith 2017), CSM

interaction also suitably explains the undulations often seen in SLSN-I light curves (LCs), which are not naturally predicted by the magnetar scenario (but see Moriya et al. 2022). For some events, a combination of these two mechanisms was suggested as powering mechanism (e.g., Fiore et al. 2021; Hosseinzadeh et al. 2022; Chen et al. 2023b; West et al. 2023). Another possibility considers that SLSNe are the result of a pair instability SN (PISN) explosion, in which a very massive progenitor (with a He-core mass  $64 \text{ M}_\odot \lesssim M_{\text{He core}} \lesssim 133 \text{ M}_\odot$ , Heger & Woosley 2002) collapses due to the onset of  $(e^-, e^+)$  pair production and allows for a massive production of  $^{56}\text{Ni}$ . This mechanism is in principle capable of reproducing very bright and long-lived SNe, with spectra suppressed on the blue side due to the high opacities of the Fe-group elements (e.g., Mazzali et al. 2019). For these reasons, some PISN candidates (e.g., Gal-Yam et al. 2009; Nicholl et al. 2013; Tinyanont et al. 2023) have been reinterpreted under the assumption of the magnetar scenario (Nicholl et al. 2013; Chen et al. 2015; Tinyanont et al. 2023). Conversely, the PISN model has been invoked by Schulze et al. (2024) to explain the superluminous SN 2018ibb.

Observationally, SLSNe are classified as Type II and Type I SLSNe depending on whether their spectra show Balmer lines or not (Gal-Yam 2012). In this work, we focus on hydrogen-poor events. Their LCs are very heterogeneous and continuously span between very slow or very fast evolving timescales (see e.g., De Cia et al. 2018; Inserra 2019). In addition, LCs of SLSNe I can show bumps before and/or after maximum whose amplitude is

\* Corresponding author: achille.fiore@inaf.it

usually  $< 1$  mag (e.g., Nicholl et al. 2015, 2016; Inserra et al. 2017; Lunnan et al. 2018; Angus et al. 2019; Fiore et al. 2021; Gutiérrez et al. 2022; Lin et al. 2023; Chen et al. 2023a; West et al. 2023). Moreover, spectra of SLSNe I around maximum are usually hot ( $\sim 15,000 - 20,000$  K) and often present prominent absorptions around  $3000 - 5000$  Å, which are usually interpreted as O II features (Quimby et al. 2018, but see Könyves-Tóth et al. 2020, for an alternative explanation). However, SLSNe I do not always exhibit these features (Könyves-Tóth & Seli 2023), and Saito et al. (2024) shown that their occurrence depends on their photospheric temperature. 15 – 20 rest-frame days after maximum, the spectra of SLSNe I look remarkably similar to those of SNe Ic at maximum luminosity (see e.g., Gal-Yam 2019; Inserra 2019). SLSNe I hosts are usually metal-poor and star-forming dwarfs sharing some similarities with those harboring long gamma-ray bursts (e.g. Chen et al. 2013, 2017; Lunnan et al. 2014; Leloudas et al. 2015; Perley et al. 2015; Schulze et al. 2018, 2021; Taggart & Perley 2021; Cleland et al. 2023).

A fraction of SLSNe I show spectral features of helium. In some of them, the He I  $\lambda 10830$  line has been identified in post-maximum NIR spectra and such SNe have been sometimes classified as SLSNe Ib<sup>1</sup> (see e.g., Quimby et al. 2018; Yan et al. 2020; Kumar et al. 2025). Interestingly, Chen et al. (2023b) found that all the best densely sampled LCs of SLSNe Ib presented in Yan et al. (2020) either show LC rebrightenings<sup>2</sup> (see also Zhu et al. 2023) or are better described by a hybrid  $^{56}\text{Ni}$ -decay + CSM-interaction model. This suggests a link between He-lines detections, bumps occurrence and CSM interaction in SLSNe. However, the current sample remains too small to draw firm conclusions about this. Therefore, it is crucial to expand and systematically study the sample of SLSNe Ib in order to constrain the nature of SLSN I(b) progenitors and their powering mechanisms.

In this work, we present and interpret the data of the observational campaign of the SLSN Ib SN 2021bnw, whose Helium abundance was inferred from the analysis of a near-infrared (NIR) spectrum observed 87 days after maximum. SN 2021bnw was located at R.A. =  $10^{\text{h}}53^{\text{m}}52^{\text{s}}.18$ , Dec. =  $+12^{\circ}33'29''.12$ , at a redshift  $z = 0.0888 \pm 0.0004$  (see Sec. 3) and was discovered by Fremling (2021) within the Zwicky Transient Facility (ZTF; Graham et al. 2019; Bellm et al. 2019b) and classified as a hydrogen-poor SLSN I by Magee et al. (2021) within the advanced (extended) Public ESO Spectroscopic Survey of Transient Objects (ePESSTO+, Smartt et al. 2015). SN 2021bnw is not grouped among the brightest SLSNe I as its absolute magnitude in the optical bands is  $-20.7$  mag (see Sec. 2) and it was included by Gomez et al. (2022) in a sample of ‘luminous SNe’, i.e. SNe with an absolute peak magnitude between classical core-collapse SNe and the faintest SLSNe. In addition, Pursiainen et al. (2023) and Poidevin et al. (2023) included SN 2021bnw in two polarization studies, both of which suggest that no significant departure from spherical symmetry for this event. Finally, Necker et al. (2022) initially included SN 2021bnw in a sample of possible counterpart of the high-energy neutrino IceCube (Aartsen et al. 2014, 2015) Alert IC200109A (Garrappa et al. 2020), but then it was not recognized as a viable candidate.

Hereafter, in Sec. 2, we discuss the observed and the bolometric LCs of SN 2021bnw; in Sec. 3, we present the optical and

NIR spectra of SN 2021bnw; in Sec. 4, we compare the spectro-photometric data of SN 2021bnw in the context of SLSNe I and we discuss a possible model for its interpretation; finally, we present our conclusion in Sec. 5. Throughout the paper, we will assume a flat Universe with  $\Omega_M = 0.31$ ,  $\Omega_\Lambda = 0.69$  and with a Hubble constant  $H_0 = 70.5 \pm 2.37 \text{ km s}^{-1} \text{ Mpc}^{-1}$  (Khetan et al. 2021).

## 2. Observed and bolometric light curves

We obtained the optical/NIR photometry of SN 2021bnw with an extensive photometric follow-up campaign using several facilities, and we reduce imaging data with dedicated pipelines or the reduction package `ecsnappy` (see Appendix A.1 for a detailed description). We estimate the epoch of maximum luminosity by performing a polynomial fit around the pre-maximum and post-maximum epochs and find that the maximum luminosity of SN 2021bnw occurred in  $g$  band on MJD =  $59269.12 \pm 0.01$  at  $g = 17.38 \pm 0.01$  mag. The errors on the peak magnitude and of the maximum-luminosity epoch are evaluated by varying the degree of the polynomial. After measuring the redshift by means of the narrow emission lines from the host galaxy (see Sec. 3), we obtain the luminosity distance  $d_L = 402.5 \pm 17$  Mpc. As we identify no narrow absorption interstellar line of the Na ID doublet in the optical spectra, we assume the host attenuation to be negligible (Poznanski et al. 2012). Given the distance modulus  $\mu = 38.02 \pm 0.10$  mag and the Galactic absorption  $A_V = 0.05$  mag (Schlafly & Finkbeiner 2011), we compute the absolute peak  $g$  magnitude  $M_g = -20.70 \pm 0.10$  mag. Moreover, we obtain the pseudo-bolometric LC in the following way: for each epoch and filter, we convert the multicolor photometry in flux, thus retrieving the spectral energy distribution (SED). We then integrate over the wavelength using the trapezoidal rule and assuming zero flux outside the integration boundaries. Finally, for each epoch the pseudo-bolometric luminosity is obtained by multiplying the integrated flux by  $4\pi d_L^2$ . The errorbars on the pseudo-bolometric LC are estimated combining the photometric error and the error on the luminosity distance. The pseudo-bolometric LC is computed adopting the epochs of the  $g$ -filter LC as a reference since it is the most densely sampled (Table B.1), and missing coeval magnitude measurements in other filters are estimated by interpolation (or extrapolation, if necessary) assuming constant color. Our calculation of the pseudo-bolometric LC of SN 2021bnw does not include UV magnitudes. In fact, due to the lack of bright stars in the field causing a spacecraft safety issue, it was not possible to trigger the *Swift*/UVOT telescope (Gehrels et al. 2004) for SN 2021bnw.

The multi-band LCs of SN 2021bnw are shown in Fig. 1. The pre-maximum detections are scarce but enable us to constrain the rest-frame rise time towards the maximum luminosity. Given the last ZTF- $g$  detection limit at a phase  $\approx -40$  rest-frame days (MJD = 59225.4) before maximum and the first ZTF detection at a phase  $\approx -38$  rest-frame days (MJD = 59227.4) before maximum, we estimated a rise time for the  $g$ -filter LC of about 39 days. Soon after maximum luminosity, the LCs show a linear declining phase lasting about 80 rest-frame days during which the optical LCs present two possible rebrightenings. In Fig. 1 (right panel), for each of the best-sampled LCs ( $B, V, g, r$ ) we subtract the best-fit first-order polynomial between 5 and 80 days (excluding the epochs in which the bumps occur) and we recognize two deviations from the linear trend. The first one peaks at about 35 days and has an amplitude  $\lesssim 0.25$  mag in the  $B$  filter and slightly decreases in the redder ones. The second one is seen in  $B$  and  $V$  filters only around 70 – 80 days, but with a slightly

<sup>1</sup> In the case of PTF10hgi, it has been also referred to as SLSN IIb due to the hydrogen and helium richness of its spectrum (Quimby et al. 2018; Gal-Yam 2019).

<sup>2</sup> A similar association has also been seen in some normal stripped-envelope SNe (see e.g. Sollerman et al. 2020).

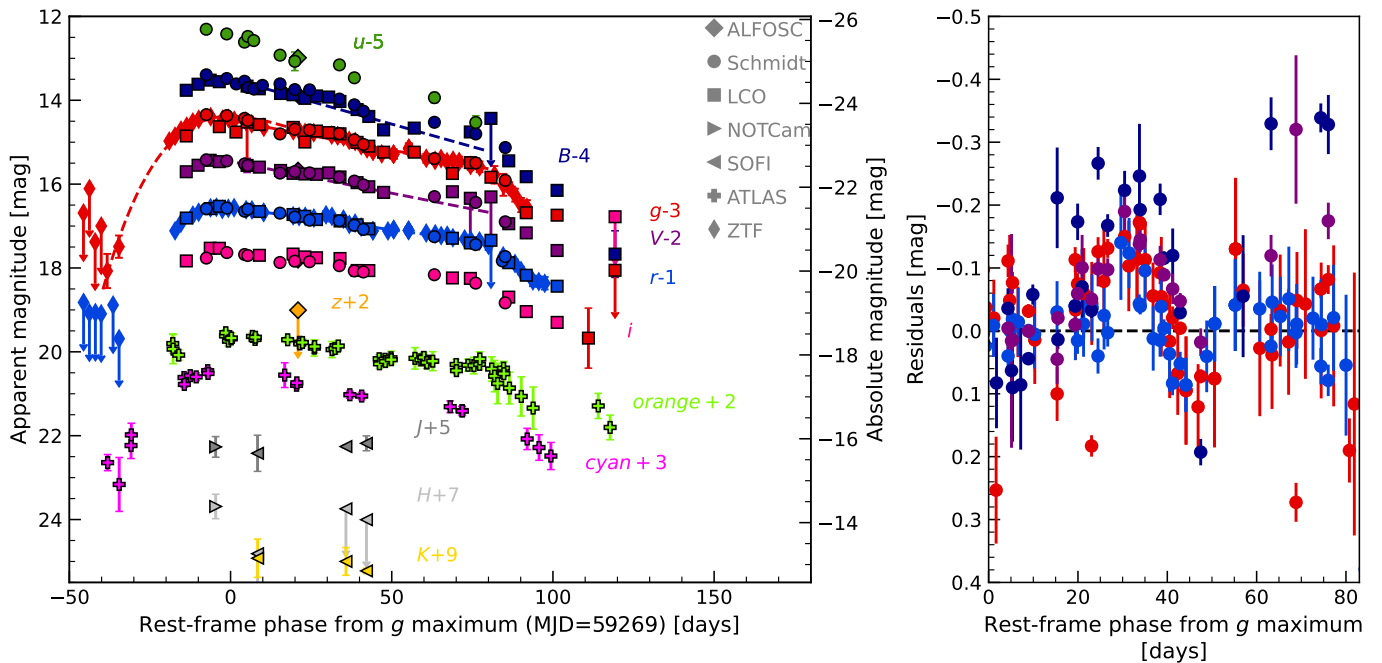


**Fig. 1.** Left panel:  $u$ -,  $B$ -,  $g$ -,  $V$ -,  $r$ -,  $i$ -, ATLAS *cyan*-, ATLAS *orange*-,  $z$ -,  $J$ -,  $H$ -,  $K$ -filter LCs (green, dark blue, red, purple, blue, magenta, orange, light green, violet, dark gray, light gray, yellow symbols) of SN 2021bnw. LCs are displayed in apparent (left axis) and absolute magnitude (right axis) and are shifted by a constant (shown in the label). The dashed line shows the polynomial fit used to estimate the maximum luminosity epoch. LCs in different filters are colored with different colors as labelled to their right side. Different symbols correspond to different instruments, as labelled in gray on the top right corner. Magnitudes are reported in the AB magnitude system. Right panel: residuals after the subtraction of the best-fit one-dimensional polynomial between 2 and 80 days after maximum luminosity in  $B$ ,  $g$ ,  $V$ ,  $r$  bands. The dashed black line marks the zero-residual level for reference. In this panel, the dots are colour-coded as in the left panel and the detection limits were removed for visualization purpose.

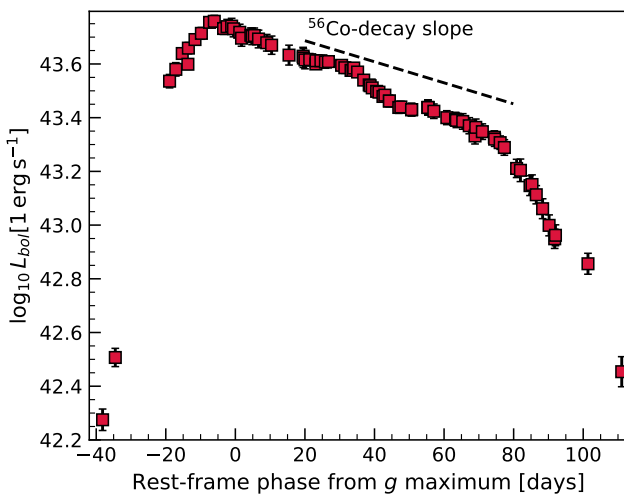


**Fig. 2.** Pseudo-bolometric LC of SN 2021bnw. The  $^{56}\text{Co}$  slope is shown for comparison purpose.

larger amplitude of  $\lesssim 0.3$  mag in  $B$  band and a comparable one in  $V$  band (if we neglect the two  $V$  detections with higher error-bars, see Fig. 1, right panel). After this phase, the LCs steepen for about 30 days, after which the SN set behind the Sun and thereafter it faded beyond the detection limit. The pseudo-bolometric LC of SN 2021bnw is shown in Fig. 2. Around the maximum luminosity, it exhibits a wedge-shaped rise and decline, which is

not novel among SLSNe I (see Sect. 4.1), and overall it reproduces the behavior of the multiband LCs in  $g$ ,  $r$  filters. The average slope of the post-maximum declining phase within 80 days of the bolometric LC of  $\approx 0.016 \text{ mag d}^{-1}$  is faster than the  $^{56}\text{Co}$ -decay slope assuming full  $\gamma$ -ray trapping. During this phase, the pseudo-bolometric LC slightly oscillates at  $\approx 40$  days but the second bump at  $\sim 75$  days (see Fig. 2) is not evident or possibly blends with the declining knee after which the LC declines with a slope of  $\approx 0.07 \text{ mag d}^{-1}$ .

### 3. Optical and NIR spectra

We obtained the optical spectroscopy of SN 2021bnw with an extensive photometric follow-up campaign using different facilities, and we reduced the raw spectroscopic frames with standard *IRAF* routines or dedicated pipelines (see Appendix A.2 for a detailed description). The spectral evolution of SN 2021bnw is shown in Fig. 3. The hot ( $\sim 14,000 - 17,000$  K) pre-maximum/maximum spectra show the  $\text{O II}$  and the  $\text{Ca II H \& K}$  features on the blue side and a broad  $\text{C II } \lambda\lambda 6580, 7121$ ,  $\text{O I } \lambda 7774$  lines on the red one.  $\text{O II}$  lines are not seen in the almost featureless spectrum observed at 7 days after maximum, although the lower signal-to-noise ratio of the blue side does not rule out their contribution. On day 16, the  $\text{Si II } \lambda 6355$  line also appears and on days 25, 31 the spectral continuum suddenly becomes bluer compared to day 21, approximately coeval with the first LC bump. It is not clear whether this also happens at 70 – 80 days, when the second bump appears in the  $B$ ,  $V$  LCs, or if it is an artifact of the lower signal-to-noise ratio on the blue side of the spectrum. As noted in the case of SN 2017gci (Fiore et al.

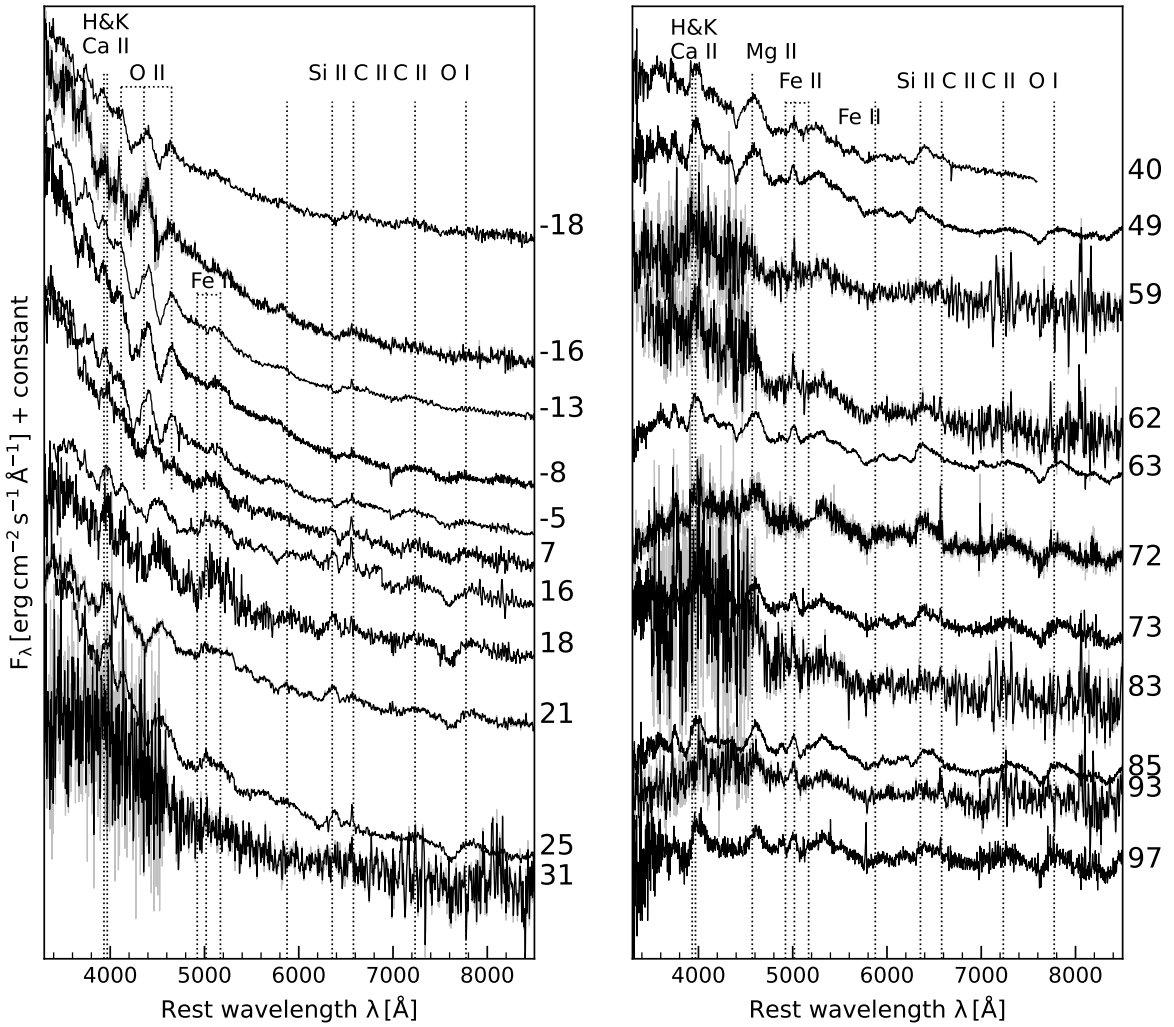


**Fig. 3.** Spectral evolution of SN 2021bnw. The dotted lines mark the line identifications labelled on their top and refer to the emission component at rest frame. On the right side of each spectrum the rest-frame phase with respect to the  $g$ -band maximum luminosity is reported (in days). The spectra at phases  $-12, 25, 35, 62, 72, 86$  and  $96$  have been re-binned (with a bin size of  $5 \text{ \AA}$ ) and smoothed with a Savitzky-Golay filter for visualization purpose.

2021) showing two bumps in the post-maximum LC, no noticeable change are seen in the spectra during the epochs at which the bumps appear. Then, on day 31, the spectrum lacks any discernible features and gradually transitions into a new phase mirroring the spectrum of a SN Ic at its maximum luminosity. This can be seen from the emergence of the Mg II at about  $\sim 4570 \text{ \AA}$  and Fe II features between  $4500 - 5500 \text{ \AA}$ . In particular, in the spectrum at 40 days after maximum, a broad feature at  $\approx 5010 \text{ \AA}$  appears, which we tentatively interpret as Fe II  $\lambda 5018$ , although the other lines of the triplet ( $\lambda\lambda\lambda 4923, 5018, 5169$ ) are not seen or possibly blended. These features are seen until day 97 when the spectrum is still photospheric, while the continuum gradually cools and the O I  $\lambda 7774$  becomes more pronounced. At the latest phases, the narrow emission lines from the host galaxy start to be seen. We measure the redshift of the host galaxy of SN 2021bnw

using the narrow H $\alpha$  and obtained  $z = 0.0888 \pm 0.0004$  fitting a gaussian to the line profile. We use the absorption minima of O I P-Cygni profiles to estimate the O I velocity of SN 2021bnw (see Fig. 4). In detail, we fit a Gaussian to the absorption profiles and measure the shift compared to the rest-frame emission wavelength. In addition, we estimate the expansion velocity from the blackbody radius (see Sec. 4.1.1), which approximately follows a power law with an index  $-2/3$  (see Fig. 4). Both velocities agree within  $\sim 20$  days after maximum. After that, the O I velocity remains nearly constant at  $\sim 7500 \text{ K}$  while the blackbody one still follows the power-law behavior. From this comparison, we broadly constrain the initial photospheric velocity to  $\sim 10,000 - 7,000 \text{ km s}^{-1}$  at pre-maximum/maximum epochs. The NIR spectrum (see Fig. 5, left panel) shows five absorptions between  $0.9 - 1.3 \mu\text{m}$  which are usually seen in the

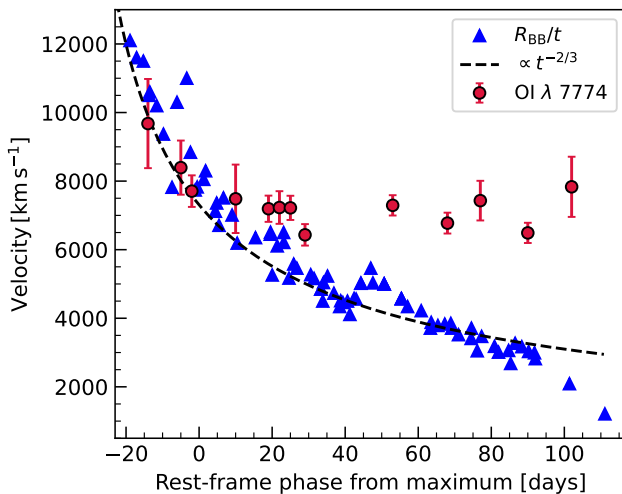


**Fig. 4.** Velocities of SN 2021bnw measured fitting a gaussian to the absorption minima of the  $\text{OI } \lambda 7774$  (red dots) and from the blackbody radius  $R_{\text{BB}}$  (blue triangles, see Fig. 10). For comparison, we also plot a  $\propto t^{-2/3}$  curve (dashed black line).

NIR spectra of stripped-envelope SNe (e.g., Shahbandeh et al. 2022). However, given the high expansion velocities some features are likely blended and their identification can be challenging. This is true in particular for the prominent P-Cygni feature at  $\sim 1.1 \mu\text{m}$ . A Gaussian fit of its emission component is peaked at  $\lambda \simeq 1.095 \mu\text{m}$  and points at the contribution of  $\text{Mg II } \lambda 1.0927 \mu\text{m}$  (see Fig. 5, right panel). A closer inspection of the blue wings of the emission (Fig. 5, right panel) draws attention to a possible inflection about  $\sim 1.08 \mu\text{m}$ , likely owed to the contribution of the  $\text{He I } \lambda 1.083 \mu\text{m}$  P-Cygni profile. Moreover, on the red wing of the emission component at  $1.1 \mu\text{m}$ , we tentatively identify the weak bump as  $\text{O I } \lambda 1.1290 \mu\text{m}$  and the following absorption as  $\text{Mg I } \lambda 1.1828 \mu\text{m}$ , while bluewards of it we identify the contribution of  $\text{O I } \lambda 0.9264 \mu\text{m} + \text{Mg II } \lambda 0.9227 \mu\text{m}$  and  $\text{Mg II } \lambda 1.0092 \mu\text{m}$ . Finally, the identification of the  $\text{He I}$  line is corroborated by the weaker absorption at  $\sim 2.02 \mu\text{m}$ , which is compatible with  $\text{He I } \lambda 2.0581 \mu\text{m}$  (see also Sec. 3.1). However, optical  $\text{He I}$  lines like the  $\lambda 5876$  usually seen in SNe Ib are not clearly distinguished in the spectra of SN 2021bnw but they are likely blended with iron/magnesium features (see also Sec. 3.1). In any case, the relative weakness of the  $\text{He I } \lambda 5876$  feature does not necessarily invalidate the  $\text{He I}$  identification in the NIR spectrum (see e.g. Teffs et al. 2020).

### 3.1. Synthetic spectra calculation with TARDIS

To test the proposed line identifications in the NIR spectrum of SN 2021bnw, we compute a synthetic spectrum using the Monte Carlo radiative-transfer code TARDIS (Kerzendorf & Sim 2014). TARDIS is an open-source, one-dimensional code widely used for the rapid spectral synthesis of supernovae. Despite some simplifying assumptions like spherical symmetry and homologous expansion, TARDIS is capable of consistently describing the plasma state and handling radiation-matter interactions. It defines a computational domain in velocity space with a fixed inner boundary, representing the SN photosphere. From this boundary, a blackbody radiation field propagates and interacts with the overlying ejecta.

|                       |  |
|-----------------------|--|
| luminosity requested  | $1.65 \times 10^{43} \text{ erg s}^{-1}$ |
| time_explosion        | 126 days                                 |
| $\rho_0$              | $3.4 \times 10^{-9} \text{ g cm}^{-3}$   |
| $v_0$                 | $10000 \text{ km s}^{-1}$                |
| $t_0$                 | 1 day                                    |
| exponent              | -4                                       |
| ionization            | nebular                                  |
| excitation            | dilute-lte                               |
| radiative rates type  | dilute-blackbody                         |
| line interaction type | downbranch                               |
| helium treatment      | recomb-nlte                              |

**Table 1.** TARDIS configuration used for the synthetic spectrum in Fig. 6.

In detail, for the spectrum calculation we use the TARDIS built-in power-law density profile  $\rho(v, t) = \rho_0(t/t_0)^{-3}(v/v_0)^{-\alpha}$ . We infer  $\alpha = 4$  from the velocity evolution (see Sec. 3) using a formalism similar to Nicholl (2026, see equation 4 therein),  $v_0 = 10000 \text{ km s}^{-1}$  and fix  $\rho_0 = 3.4 \times 10^{-9} \text{ g cm}^{-3}$ . The last two parameters were varied to obtain a TARDIS ejecta mass lower or similar to that reported in Sec. 4.2. The other TARDIS simulation parameters are set up following Williamson et al. (2021) and Boyle et al. (2017), and are summarized in Table 1. We adopt a homogeneous abundance profile and the latest version (March 2025) of the TARDIS atomic-data file (Kurucz 2017). In addition to helium, we input the chemical elements responsible for the lines identified in the optical spectra and vary their abundances to fit the NIR spectrum of SN 2021bnw. To this aim, we also use the optical spectrum at 85 days as an additional reference and explored the TARDIS-parameter space to provide a good compromise between the optical and NIR spectral regions. However, we emphasize that we do not attempt to model the entire the spectrum, but only to test the helium-lines identification. The observed NIR spectrum is compared with the synthetic TARDIS spectrum in Fig. 6. The TARDIS spectrum predicts the contribution of  $\text{He I}$  to the absorption at  $1.05 \mu\text{m}$  although it partly overlaps with  $\text{Mg II}$ . By contrast, helium alone reproduces the absorption at  $2 \mu\text{m}$  reasonably well (see Fig. 6, right panel). Since this region is expected to experience minimal contamination from other features (Shahbandeh et al. 2022), we can more confidently attribute contributions in the NIR spectrum of SN 2021bnw to helium.

## 4. Discussion

### 4.1. Photometric and spectroscopic comparisons with other SNe

We select a sample of SLSNe Ib to compare the photometry and spectra of SN 2021bnw with those of analogous objects having post-maximum He-rich NIR spectra: PTF10hgi, SN 2012il (Inserra et al. 2013) and SN 2017egm (Nicholl et al. 2017a; Bose et al. 2018; Hosseinzadeh et al. 2022; Zhu et al. 2023) and SN 2019hge (Yan et al. 2020). We also add to the comparison sample the SLSN I SN 2020wnt (Gutiérrez et al. 2022), which has possible  $\text{He I}$  detections at about  $\sim 5000$  and  $\sim 7000 \text{ \AA}$  and has a similar steepening in the LC. We compare the  $K$ -corrected absolute LCs in all available filters for the SNe of the comparison sample (Fig. 7). For SN 2021bnw, we use the  $K$ -correction following Fiore et al. (2021) (see Table B.3), while for the other SNe we use the approximation  $K = -2.5 \log_{10}(1+z)$  (Hogg et al. 2002), which is reasonable for SLSNe I (Chen et al. 2023a). Interestingly, SN 2021bnw and SN 2017egm are

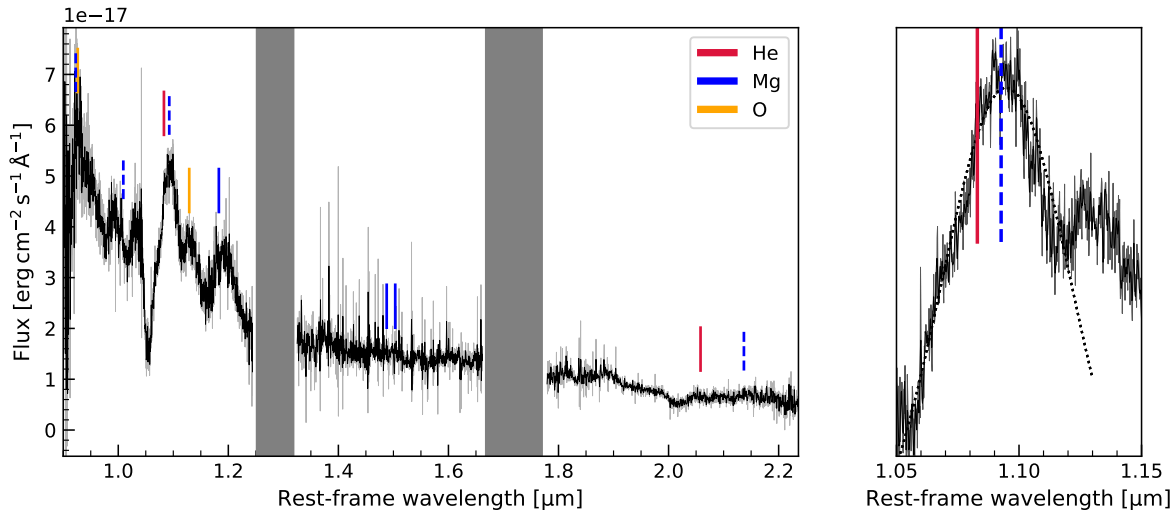


**Fig. 5.** Left panel: NIR spectrum of SN 2021bnw at 87 days after maximum. The grey-shaded areas mark the regions contaminated by telluric absorptions. Right panel: same as the left panel but zooming the region close to  $1.1\text{ }\mu\text{m}$ . In both of them, the wavelengths corresponding to the emission components of the NIR features from Helium, Magnesium and Oxygen are marked with different colors (see the legend on the top-right corner), solid and dashed lines correspond to neutral and singly-ionized ones, respectively.

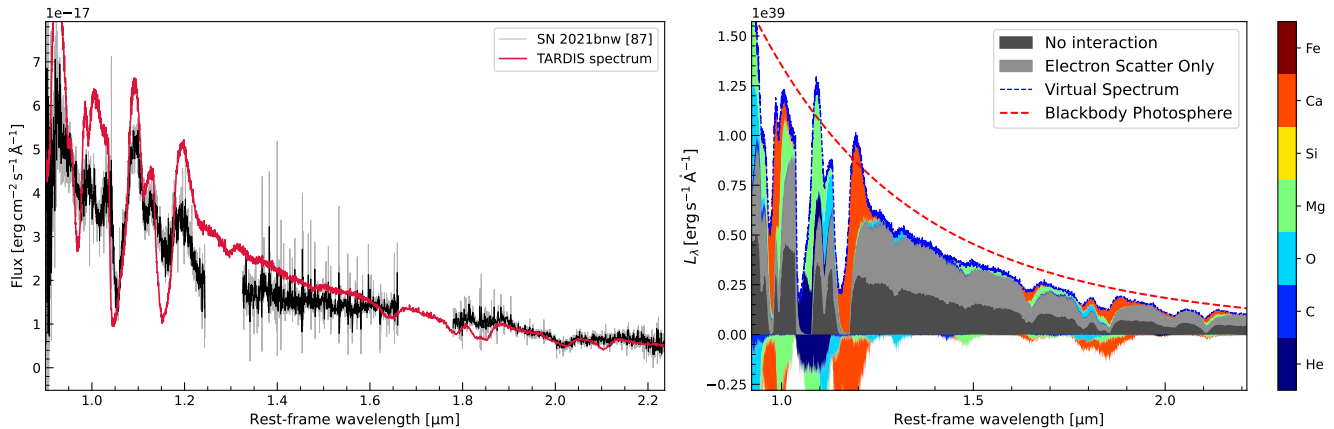


**Fig. 6.** Left panel: Comparison of the NIR spectrum of SN 2021bnw at 87 days after maximum with the TARDIS synthetic spectrum. Right panel: spectral decomposition (SDEC) plot (Kromer et al. 2013) where different contributions to emission and absorption of quanta in the TARDIS Monte Carlo simulation are colored as in the palette.

remarkably similar in terms of absolute magnitude around the pre-maximum/maximum and early post maximum epochs ( $\lesssim 20$  days), in which the LCs of both SNe present a wedge shape which is sharper in  $g$  and broader in other filters. However, SN 2017egm rises faster towards the maximum compared to SN 2021bnw (see Fig. 7). After  $\sim 20$  days the follow-up of SN 2017egm was interrupted, but soon after  $\sim 85$  days their  $g$  LCs are still similar until  $\sim 100$  days. Compared to them, the other SLSNe I of the sample evolve faster after maximum in  $g$  and show a change of slope about 50 days after maximum. In particular, SN 2019hge exhibits a sharp bump at that epoch, which precedes of  $\sim 10$  days a similar one in the  $g$  LC of SN 2021bnw.

We also compared four representative spectra of SN 2021bnw with those of the SNe of the comparison sample at comparable phases (see Fig. 8, 9) after having corrected them for redshift and Galactic extinction following Schlafly &

Finkbeiner (2011). The spectra were obtained via Wiserep<sup>3</sup> (Yaron & Gal-Yam 2012). The spectra of SN 2021bnw look more similar in terms of features and spectral continuum to those of SN 2019hge, SN 2017egm and SN 2012il. However, SN 2012il evolves faster than SN 2021bnw and reaches the featureless phase before SN 2021bnw (see Fig. 3). The spectra of SN 2020wnt are redder and with stronger features at post-maximum epochs. Finally, we compared the NIR spectrum of SN 2021bnw with two spectra of SN 2017egm and SN 2012il, although at different rest-frame phase with respect to maximum. In the three spectra (see Fig. 9), a feature is seen at about  $\sim 1.1\text{ }\mu\text{m}$ , although with different characteristics. In fact, while in the case of SN 2012il it looks like a pure emission feature, in the case of SN 2021bnw and SN 2017egm a P-Cygni profile is present with a broader blue wing compared to the red one. The  $\text{O I } \lambda 0.9264\text{ }\mu\text{m} + \text{Mg II } \lambda 0.9227\text{ }\mu\text{m}$  feature is probably present

<sup>3</sup> <https://www.wiserep.org>.

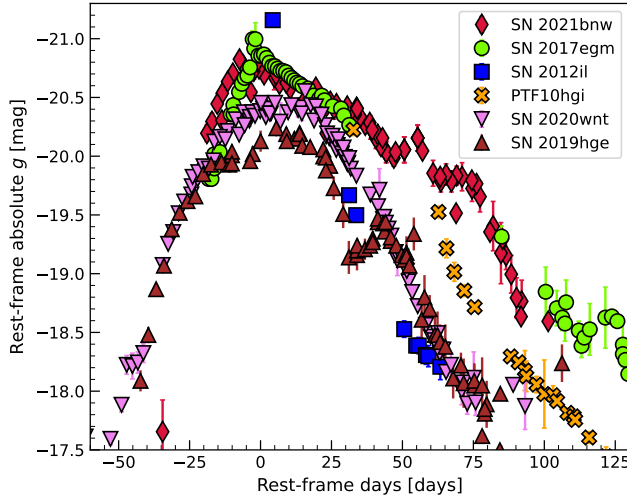


**Fig. 7.** Comparisons of the  $K$ -corrected  $g$ -band absolute LCs of SN 2021bnw with those of the comparison sample. The LCs of the selected SNe are marked differently as explained in the caption on the top.

in the NIR spectra of SN 2012il and SN 2017egm, while the  $O\,\text{I}$  and  $Mg\,\text{II}$  features are identified in that of SN 2017egm only, since this wavelength range is not covered by the spectrum of SN 2012il. However, due to the low signal-to-noise ratio of the spectrum of SN 2012il and the considerable phase shift with respect to maximum, we cannot exclude that these SNe shared more or fewer spectral properties at coeval epochs.

#### 4.1.1. Blackbody temperature and radius

We compare the blackbody radius and temperature of SN 2021bnw with those of the other SNe of the sample considered in this work. For consistency, we use the same script to integrate the multi-band photometry and to retrieve the blackbody temperature and radius adopted for SN 2021bnw. We computed the evolution of the blackbody temperature and radius by fitting a Planck's law to the SED (see Fig. 10, top and bottom panel, respectively) and using the Stefan-Boltzmann law.

The early measurements of both blackbody temperature and radius of SN 2021bnw are in good agreement with those of SN 2017egm. The apparent plateau behavior before maximum of SN 2021bnw is not reliable. In fact, these epochs are not very well sampled except in the  $g$  and *cyan* filters (see Fig. 1), where the SED was extrapolated assuming constant color in cases of missing coeval magnitude measurements in the other bands. The same is true for SN 2012il. After maximum, the blackbody temperatures of all the SNe smoothly decline at comparable rates towards an almost constant plateau. Such a 7,000–8,000 K ‘temperature floor’ (Inserra et al. 2013; Nicholl et al. 2017b) is quite common among SLSNe I and has been ascribed to the oxygen recombination. This interpretation might be questioned for SN 2020wnt, as it also presents a temperature floor but it does not show the prominent W-shaped  $O\,\text{II}$  features around its maximum-luminosity epoch. Similarities are also seen in the evolution of the blackbody radius (see Fig. 10, bottom panel) which, in the case of SN 2021bnw, culminates its expansion phase about three days after maximum luminosity and, as for the temperature, broadly agrees with the blackbody radii of SN 2017egm and SN 2012il up to  $\sim 40$  days after maximum.

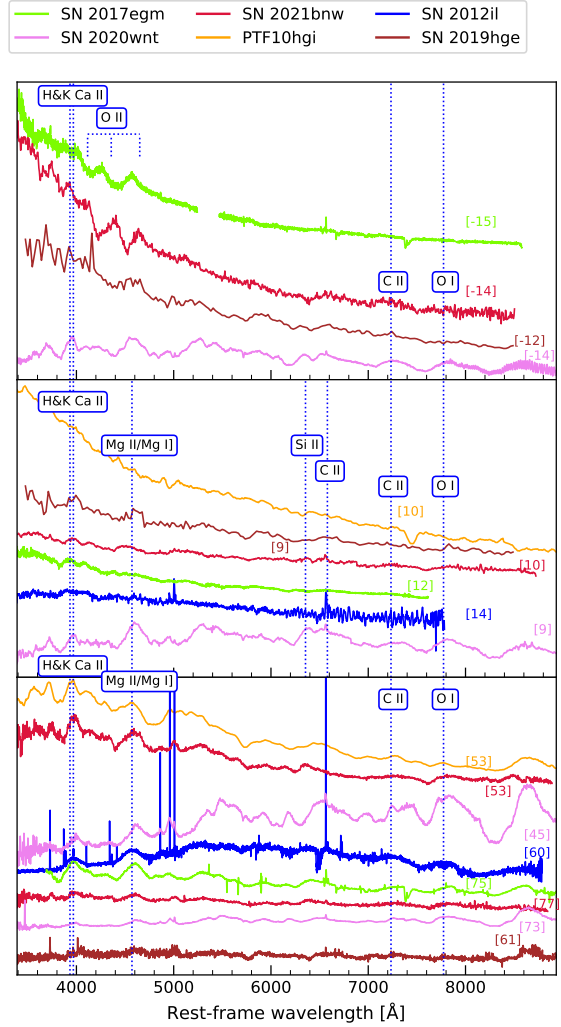


**Fig. 8.** Comparison of optical spectra of SN 2021bnw with those of the comparison sample (see text for details) at different phases: pre-maximum (top panel), post maximum (within 15 days after maximum, middle panel), post maximum (within 80 days after maximum, bottom panel). The rest-frame phase from maximum of each spectra is labeled between square brackets on the right side of each spectrum. The rest-frame wavelength of some transitions are marked with blue dotted lines.

We caution that the measurements of blackbody temperatures and radius for SN 2021bnw might be inaccurate due to the lack of UV photometry.

#### 4.2. Exploring a scenario for SN 2021bnw

Several properties deduced for SN 2021bnw in the previous sections like luminosity, photospheric velocity and spectral evolution are consistent with those of the bulk SLSN-I population (see e. g. Aamer et al. 2025). These arguments provide a guess for outlining the explosion scenario of SN 2021bnw. Following the approach adopted for its close sibling SN 2017egm (see Sec. 4.1), we consider a scenario involving the combination of a central heating source and CSM interaction. In fact, in both cases this hypothesis is supported by the sudden decline happen-

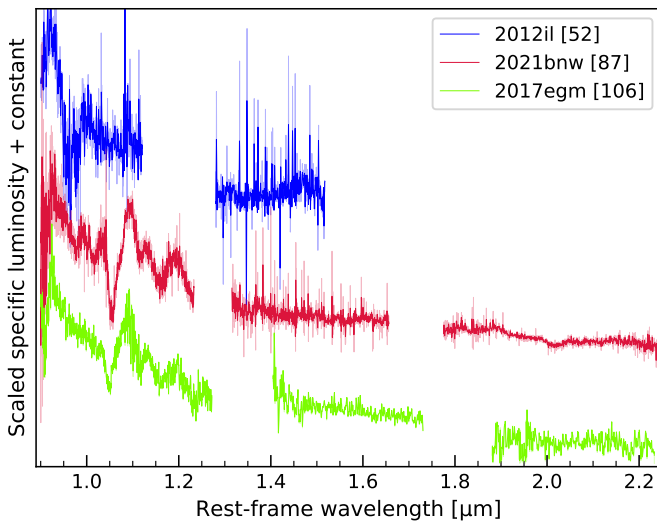


**Fig. 9.** Same as Fig. 8, but for NIR spectra. The spectra of SN 2012il and SN 2021bnw are smoothed with a Savitzky-Golay filter. For visualization purpose, the spectrum of SN 2012il was also rebinned due to its low signal-to-noise ratio.

ing  $\sim 80$  days after maximum, potentially marking the breakout of the forward shock out of the CSM (e. g. Chevalier 1982; Chatzopoulos et al. 2012).

Considering a  $^{56}\text{Ni}$ +CSM scenario, Wheeler et al. (2017) found for SN 2017egm a  $^{56}\text{Ni}$  mass  $M(^{56}\text{Ni}) = 0.15 M_{\odot}$ , an ejecta mass  $M_{\text{ejecta}} = 10.7 M_{\odot}$  and a CSM mass  $M_{\text{CSM}} = 2.7 M_{\odot}$  using the module `csmrads0` of `TigerFit` (Chatzopoulos et al. 2013). This code computes synthetic SN LCs exploiting the diffusion scheme introduced by Arnett (1980, 1982) for a variety of power mechanisms. Similarly, Zhu et al. (2023) used the same tool but on a more extended pseudo-bolometric LC and found  $M(^{56}\text{Ni}) = 1 M_{\odot}$ ,  $M_{\text{ejecta}} = 30 M_{\odot}$  and  $M_{\text{CSM}} = 0.8 M_{\odot}$ . We do not perform a fit with `csmrads0` as the LCs of SN 2017egm and SN 2021bnw almost overlap around maximum (Fig. 7) and we expect similar parameter estimates. However, although semi-analytic diffusion schemes can capture the general features of the observed LCs, their inferred physical quantities may substantially differ from those obtained with detailed radiative-transfer calculations (see e.g. Moriya et al. 2013). Kozyreva et al. (in preparation) will present radiative-transfer calculations with the code `STELLA` (Blinnikov et al. 1998, 2000) to improve the reliability of the predictions on the physical parameters of the explosion. They will also discuss in more detail the model and a systematic exploration of the parameter space for SN 2021bnw. In detail, their calculations converge on an ejecta mass of  $\approx 15 - 20 M_{\odot}$ , a CSM mass of  $\approx 7 M_{\odot}$ , an explosion energy of  $\approx 5 \times 10^{51}$  erg and a  $^{56}\text{Ni}$  mass of  $\approx 1.7 M_{\odot}$ .

We show in Fig. 11 the `STELLA` model `he90d5he1m6X1W1` computed by Kozyreva et al. for a  $^{56}\text{Ni}$ +He-rich CSM scenario. This model is computed assuming  $M(^{56}\text{Ni}) = 1.7 M_{\odot}$ ,  $M_{\text{ejecta}} = 15 M_{\odot}$ ,  $M_{\text{CSM}} = 6.5 M_{\odot}$  and a kinetic energy  $E_{\text{kin}} = 3.8 \times 10^{51}$  erg. While the `STELLA` LC is able to capture the maximum/post-maximum epochs of the pseudo-bolometric LC of SN 2021bnw, it does not predict the two initial detections. Further investigation of these early-time observations, as well as of the progenitor properties of SN 2021bnw within a single-star evolutionary framework, will be presented in Kozyreva et al. (in preparation). We mention that the choice of  $^{56}\text{Ni}$  as central heating source is not supported by a specific observational evidence

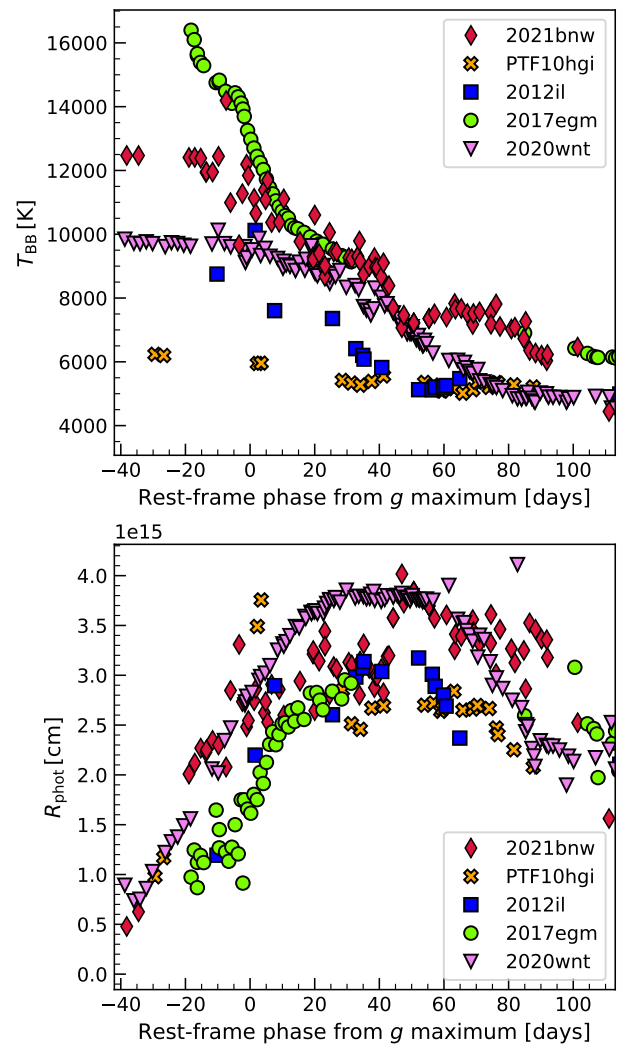


**Fig. 10.** Evolution of the blackbody temperature of SN 2021bnw  $T_{\text{BB}}$  (top) and the blackbody radius of SN 2021bnw  $R_{\text{phot}}$  (bottom). The errorbars on  $T_{\text{BB}}$  and  $R_{\text{phot}}$  are not shown for visualization purpose.

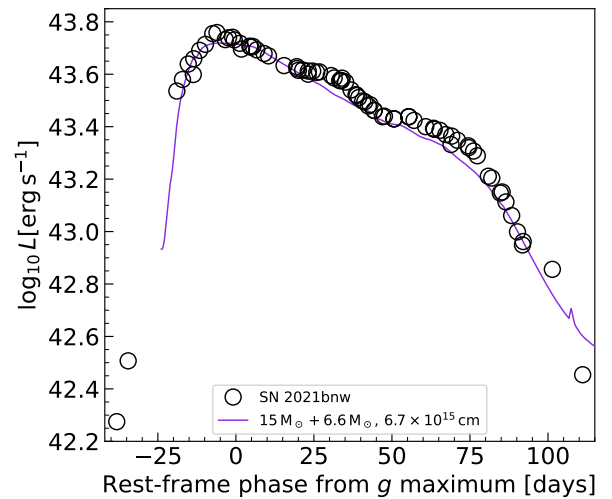


**Fig. 11.** Pseudo-bolometric LC of SN 2021bnw (open circles) compared with the `STELLA` model `he90d5he1m6X1W1` (solid purple line).

and may be replaced by an alternative energy-injection mechanism, such as e. g. the spin-down radiation lost by a newly-born magnetar (see Poidevin et al. 2023, for the application of this scenario to the case of SN 2021bnw).

We caution that the  $^{56}\text{Ni}$  mass and the kinetic energy required by the STELLA models imply a significant departure from an ordinary core collapse (see Introduction) motivating the consideration of alternative explosion channels, such as the collapsar scenario (e. g. MacFadyen & Woosley 1999) or magneto-rotational core collapse (e. g. Winteler et al. 2012; Mösta et al. 2018; Reichert et al. 2023). In principle, also a PISN is able to yield much more  $^{56}\text{Ni}$  than an ordinary core collapse, but PISN theory predicts a very slow evolving LC that does not match the observed LC of SN 2021bnw.

While we are not able to draw any conclusions in this regard, we note that, under the assumption that CSM interaction played a significant role in shaping the LC of SN 2021bnw, the absence of its clear spectroscopic signatures (see e. g. Smith et al. 2010) in the spectra of SN 2021bnw – and, in general, of SLSNe I – may point to asymmetry in the ejecta–CSM configuration (e. g. Smith 2017; Andrews & Smith 2018). Such asymmetries arise naturally in explosion scenarios involving strong rotation and magnetic fields, as expected in the aforementioned alternative core-collapse pathways.

## 5. Conclusions

SN 2021bnw joins the number of SLSNe I that exhibit helium lines in their spectra, otherwise known as SLSNe Ib. In this work, we have presented the outcome of the extensive optical/NIR spectro-photometric follow-up campaign we led for it. Specifically, its  $g$ -filter LC reaches an absolute peak magnitude of  $-20.7$  mag, placing it on the faint wing of the SLSN-I luminosity function. The optical spectra of SN 2021bnw follow the typical spectral evolution of SLSNe I and the late NIR spectrum, taken 87 days after maximum luminosity, reveals the  $\lambda 1.1\mu\text{m}$  and  $\lambda 2\mu\text{m}$  He features (see Sec. 3). We further investigate and confirm this identification with the radiative-transfer software TARDIS. Due to the step-like, abrupt evolving LC, we ascribe the presence of He spectral features to the interaction of the SN ejecta with H-devoid and He-rich CSM as it was suggested for its sibling SLSN I SN 2017egm. We have therefore modeled the LC of SN 2021bnw with the hydrodynamics radiative-transfer code STELLA as a combination of two events: *i*) the ejection of  $6 - 7\text{ M}_\odot$  of H-free and He-rich shell of the outermost layers of a massive star prior to the terminal explosion; *ii*) the actual SN explosion with an energy of  $5 \times 10^{51}$  erg, yielding  $1.7\text{ M}_\odot$  of  $^{56}\text{Ni}$  and ejecting  $15 - 20\text{ M}_\odot$  after the core collapse (Kozyreva et al. in preparation). However, we are not able to check these estimates against a thorough stellar-evolution study in the present work, and we note that a binary-progenitor scenario could also provide a viable explanation for SN 2021bnw.

**Acknowledgements.** A. F. acknowledges funding by the European Union – NextGenerationEU RFF M4C2 1.1 PRIN 2022 project “2022RJLWHN URKA” and by INAF 2023 Theory Grant ObFu 1.05.23.06.06 “Understanding R-process & Kilonovae Aspects (URKA)”. AR acknowledges financial support from the GRAWITA Large Program Grant (PI P. D’Avanzo) and from the PRIN-INAF 2022 “Shedding light on the nature of gap transients: from the observations to the models”. T.E.M.B. is funded by Horizon Europe ERC grant no. 101125877. This work makes use of observations from the Las Cumbres Observatory network. MN is supported by the European Research Council (ERC) under the European Union’s Horizon 2020 research and innovation programme (grant agreement No. 948381). Y.-Z. Cai is supported by the National Natural Science Foundation of China (NSFC, Grant No. 12303054), the National Key Research and Development Program of China (Grant No. 2024YFA161603), the Yunnan Fundamental Research Projects (Grant Nos. 202401AU070063,

202501AS070078), and the International Centre of Supernovae, Yunnan Key Laboratory (No. 202302AN360001). CPG acknowledges financial support from the Secretary of Universities and Research (Government of Catalonia) and by the Horizon 2020 Research and Innovation Programme of the European Union under the Marie Skłodowska-Curie and the Beatriu de Pinós 2021 BP 00168 programme, from the Spanish Ministerio de Ciencia e Innovación (MCIN) and the Agencia Estatal de Investigación (AEI) 10.13039/501100011033 under the PID2023-151307NB-I00 SNNEXT project, from Centro Superior de Investigaciones Científicas (CSIC) under the PIE project 20215AT016 and the program Unidad de Excelencia María de Maeztu CEX2020-001058-M, and from the Departament de Recerca i Universitats de la Generalitat de Catalunya through the 2021-SGR-01270 grant. N.E.R. acknowledges support from the PRIN-INAF 2022, ‘Shedding light on the nature of gap transients: from the observations to the models’ and from the Spanish Ministerio de Ciencia e Innovación (MCIN) and the Agencia Estatal de Investigación (AEI) 10.13039/501100011033 under the program Unidad de Excelencia María de Maeztu CEX2020-001058-M. T.-W.C. acknowledges the financial support from the Yushan Fellow Program by the Ministry of Education, Taiwan (MOE-111-YSFMS-0008-001-P1) and the National Science and Technology Council, Taiwan (NSTC grant 114-2112-M-008-021-MY3). PB is supported by the grant RSF 24-12-00141 for modeling supernova light curves with the STELLA code. This work makes use of observations from the Las Cumbres Observatory network (LCO). The LCO team is supported by NSF grants AST-1911225 and AST-1911151. This research made use of TARDIS, a community-developed software package for spectral synthesis in supernovae (Kerzendorf & Sim 2014). The development of TARDIS received support from GitHub, the Google Summer of Code initiative, and from ESA’s Summer of Code in Space program. TARDIS is a fiscally sponsored project of NumFOCUS. TARDIS makes extensive use of Astropy and Pyne. Based on observations collected at the European organisation for astronomical research in the Southern Hemisphere, Chile, as part of ePESSTO+ (the advanced Public ESO Spectroscopic Survey for Transient Objects). Based on observations collected at the European Organisation for Astronomical Research in the Southern Hemisphere, Chile, as part of ePESSTO+ (the advanced Public ESO Spectroscopic Survey for Transient Objects Survey – PI: Inserra). ePESSTO+ observations were obtained under ESO program IDs 1103.D-0328, 106.216C and 108.220C.. The data presented here were obtained in part with ALFOSC, which is provided by the Instituto de Astrofísica de Andalucía (IAA) under a joint agreement with the University of Copenhagen and NOT. Based on observations collected at Copernico and Schmidt telescopes (Asiago, Italy) of the INAF-Osservatorio Astronomico di Padova. Based on observations made with the Gran Telescopio Canarias (GTC), installed in the Spanish Observatorio del Roque de los Muchachos of the Instituto de Astrofísica de Canarias, in the island of La Palma. Based on observations obtained with the Samuel Oschin Telescope 48-inch and the 60-inch Telescope at the Palomar Observatory as part of the Zwicky Transient Facility project. Based on observations obtained with the Samuel Oschin Telescope 48-inch and the 60-inch Telescope at the Palomar Observatory as part of the Zwicky Transient Facility project. ZTF is supported by the National Science Foundation under Grant No. AST-2034437 and a collaboration including Caltech, IPAC, the Weizmann Institute of Science, the Oskar Klein Center at Stockholm University, the University of Maryland, Deutsches Elektronen-Synchrotron and Humboldt University, the TANGO Consortium of Taiwan, the University of Wisconsin at Milwaukee, Trinity College Dublin, Lawrence Livermore National Laboratories, IN2P3, University of Warwick, Ruhr University Bochum, Cornell University, and Northwestern University. Operations are conducted by COO, IPAC, and UW. SED Machine is based upon work supported by the National Science Foundation under Grant No. 1106171. The Gordon and Betty Moore Foundation, through both the Data-Driven Investigator Program and a dedicated grant, provided critical funding for SkyPortal (van der Walt et al. 2019; Coughlin et al. 2023).

## References

- Aamer, A., Nicholl, M., Gomez, S., et al. 2025, MNRAS, 541, 2674
- Aartsen, M. G., Abraham, K., Ackermann, M., et al. 2015, Phys. Rev. Lett., 115, 081102
- Aartsen, M. G., Ackermann, M., Adams, J., et al. 2014, Phys. Rev. Lett., 113, 101101
- Anderson, J. P. 2019, A&A, 628, A7
- Andrews, J. E. & Smith, N. 2018, Monthly Notices of the Royal Astronomical Society, 477, 74
- Angus, C. R., Smith, M., Sullivan, M., et al. 2019, MNRAS, 487, 2215
- Arnett, W. D. 1980, ApJ, 237, 541
- Arnett, W. D. 1982, The Astrophysical Journal, 253, 785
- Becker, A. 2015, HOTPANTS: High Order Transform of PSF AND Template Subtraction
- Bellm, E. C., Kulkarni, S. R., Barlow, T., et al. 2019a, PASP, 131, 068003
- Bellm, E. C., Kulkarni, S. R., Graham, M. J., et al. 2019b, PASP, 131, 018002

Blagorodnova, N., Neill, J. D., Walters, R., et al. 2018, *PASP*, 130, 035003

Blinnikov, S., Lundqvist, P., Bartunov, O., Nomoto, K., & Iwamoto, K. 2000, *ApJ*, 532, 1132

Blinnikov, S. I., Eastman, R., Bartunov, O. S., Popolitov, V. A., & Woosley, S. E. 1998, *ApJ*, 496, 454

Bose, S., Dong, S., Pastorello, A., et al. 2018, *ApJ*, 853, 57

Boyle, A., Sim, S. A., Hachinger, S., & Kerzendorf, W. 2017, *A&A*, 599, A46

Buzzoni, B., Delabre, B., Dekker, H., et al. 1984, *The Messenger*, 38, 9

Cappellaro, E. 2014, *snoopy*: a package for SN photometry

Chambers, K. C., Magnier, E. A., Metcalfe, N., et al. 2016, *arXiv e-prints*, arXiv:1612.05560

Chatzopoulos, E., Wheeler, J. C., & Vinko, J. 2012, *The Astrophysical Journal*, 746, 121

Chatzopoulos, E., Wheeler, J. C., Vinko, J., Horvath, Z. L., & Nagy, A. 2013, *The Astrophysical Journal*, 773, 76

Chen, T.-W., Smartt, S. J., Bresolin, F., et al. 2013, *apJL*, 763, L28

Chen, T. W., Smartt, S. J., Jerkstrand, A., et al. 2015, *Monthly Notices of the Royal Astronomical Society*, 452, 1567

Chen, T.-W., Smartt, S. J., Yates, R. M., et al. 2017, *Monthly Notices of the Royal Astronomical Society*, 470, 3566

Chen, Z. H., Yan, L., Kangas, T., et al. 2023a, *ApJ*, 943, 41

Chen, Z. H., Yan, L., Kangas, T., et al. 2023b, *ApJ*, 943, 42

Chevalier, R. A. 1982, *ApJ*, 258, 790

Chevalier, R. A. & Fransson, C. 2003, Supernova Interaction with a Circumstellar Medium, Vol. 598 (Weiler, K.), 171–194

Chonis, T. S. & Gaskell, C. M. 2008, *AJ*, 135, 264

Cleland, C., McGee, S. L., & Nicholl, M. 2023, *MNRAS*, 524, 3559

Coughlin, M. W., Bloom, J. S., Nir, G., et al. 2023, *ApJS*, 267, 31

De Cia, A., Gal-Yam, A., Rubin, A., et al. 2018, *The Astrophysical Journal*, 860, 100

Dekany, R., Smith, R. M., Riddle, R., et al. 2020, *PASP*, 132, 038001

Fiore, A., Chen, T. W., Jerkstrand, A., et al. 2021, *Monthly Notices of the Royal Astronomical Society* [arXiv:2012.12755]

Fremling, C. 2021, Transient Name Server Discovery Report, 2021-326, 1

Gal-Yam, A. 2012, *Science*, 337, 927

Gal-Yam, A. 2019, *ARAA*, 57, 305

Gal-Yam, A., Mazzali, P., Ofek, E. O., et al. 2009, *Nature*, 462, 624

Garrappa, S., Paliya, V., & Fermi-LAT Collaboration. 2020, GRB Coordinates Network, 26728, 1

Gehrels, N., Chincarini, G., Giommi, P., et al. 2004, *ApJ*, 611, 1005

Gomez, S., Berger, E., Nicholl, M., Blanchard, P. K., & Hosseinzadeh, G. 2022, *ApJ*, 941, 107

Graham, M. J., Kulkarni, S. R., Bellm, E. C., et al. 2019, *PASP*, 131, 078001

Gutiérrez, C. P., Pastorello, A., Bersten, M., et al. 2022, *MNRAS*, 517, 2056

Heger, A. & Woosley, S. E. 2002, *ApJ*, 567, 532

Hogg, D. W., Baldry, I. K., Blanton, M. R., & Eisenstein, D. J. 2002, *arXiv e-prints*, astro

Holmbo, S., Stritzinger, M., Nowack, G., et al. 2019, *The Astronomer's Telegram*, 12661, 1

Hosseinzadeh, G., Berger, E., Metzger, B. D., et al. 2022, *ApJ*, 933, 14

Inserra, C. 2019, *Nature Astronomy*, 3, 697

Inserra, C., Nicholl, M., Chen, T. W., et al. 2017, *Monthly Notices of the Royal Astronomical Society*, 468, 4642

Inserra, C., Smartt, S. J., Jerkstrand, A., et al. 2013, *The Astrophysical Journal*, 770, 128

Kasen, D. & Bildsten, L. 2010, *The Astrophysical Journal*, 717, 245

Kerzendorf, W. E. & Sim, S. A. 2014, *Monthly Notices of the Royal Astronomical Society*, 440, 387

Khetan, N., Izzo, L., Branchesi, M., et al. 2021, *A&A*, 647, A72

Könyves-Tóth, R. & Seli, B. 2023, *ApJ*, 954, 44

Könyves-Tóth, R., Thomas, B. P., Vinkó, J., & Wheeler, J. C. 2020, *ApJ*, 900, 73

Kromer, M., Fink, M., Stanishev, V., et al. 2013, *MNRAS*, 429, 2287

Kumar, H., Berger, E., Blanchard, P. K., et al. 2025, *arXiv e-prints*, arXiv:2506.06417

Kurucz, R. L. 2017, *Canadian Journal of Physics*, 95, 825

Leloudas, G., Schulze, S., Krühler, T., et al. 2015, *Monthly Notices of the Royal Astronomical Society*, 449, 917

Lin, W., Wang, X., Yan, L., et al. 2023, *Nature Astronomy*, 7, 779

Lunnan, R., Chornock, R., Berger, E., et al. 2014, *The Astrophysical Journal*, 787, 138

Lunnan, R., Fransson, C., Vreeswijk, P. M., et al. 2018, *Nature Astronomy*, 2, 887

MacFadyen, A. I. & Woosley, S. E. 1999, *ApJ*, 524, 262

Magee, M., Terwel, J., Prentice, S., Harvey, L., & Strotjohann, N. L. 2021, Transient Name Server Classification Report, 2021-338, 1

Masci, F. J., Laher, R. R., Rusholme, B., et al. 2023, *arXiv e-prints*, arXiv:2305.16279

Masci, F. J., Laher, R. R., Rusholme, B., et al. 2019, *PASP*, 131, 018003

Mazzali, P. A., Moriya, T. J., Tanaka, M., & Woosley, S. E. 2019, *MNRAS*, 484, 3451

Moorwood, A., Cuby, J. G., Biereichel, P., et al. 1998, *The Messenger*, 94, 7

Moriya, T. J., Blinnikov, S. I., Tominaga, N., et al. 2013, *MNRAS*, 428, 1020

Moriya, T. J., Murase, K., Kashiyama, K., & Blinnikov, S. I. 2022, *MNRAS*, 513, 6210

Mösta, P., Roberts, L. F., Halevi, G., et al. 2018, *ApJ*, 864, 171

Necker, J., de Jaeger, T., Stein, R., et al. 2022, *MNRAS*, 516, 2455

Nicholl, M. 2026, *arXiv e-prints*, arXiv:2601.05363

Nicholl, M., Berger, E., Margutti, R., et al. 2017a, *ApJ*, 845, L8

Nicholl, M., Berger, E., Smartt, S. J., et al. 2016, *The Astrophysical Journal*, 826, 39

Nicholl, M., Guillochon, J., & Berger, E. 2017b, *The Astrophysical Journal*, 850, 55

Nicholl, M., Smartt, S. J., Jerkstrand, A., et al. 2013, *Nature*, 502, 346

Nicholl, M., Smartt, S. J., Jerkstrand, A., et al. 2015, *Monthly Notices of the Royal Astronomical Society*, 452, 3869

Pejcha, O. & Thompson, T. A. 2015, *ApJ*, 801, 90

Perley, D. A., Perley, R. A., Hjorth, J., et al. 2015, *ApJ*, 801, 102

Poidevin, F., Omand, C. M. B., Könyves-Tóth, R., et al. 2023, *MNRAS*, 521, 5418

Poznanski, D., Prochaska, J. X., & Bloom, J. S. 2012, *MNRAS*, 426, 1465

Pursiainen, M., Leloudas, G., Cikota, A., et al. 2023, *A&A*, 674, A81

Quimby, R. M., De Cia, A., Gal-Yam, A., et al. 2018, *The Astrophysical Journal*, 855, 2

Reichert, M., Obergaulinger, M., Aloy, M. Á., et al. 2023, *MNRAS*, 518, 1557

Rigault, M., Neill, J. D., Blagorodnova, N., et al. 2019, *A&A*, 627, A115

Saito, S., Tanaka, M., Mazzali, P. A., Hachinger, S., & Hotokezaka, K. 2024, *ApJ*, 967, 13

Schlafly, E. F. & Finkbeiner, D. P. 2011, *ApJ*, 737, 103

Schulze, S., Fransson, C., Kozyreva, A., et al. 2024, *A&A*, 683, A223

Schulze, S., Krühler, T., Leloudas, G., et al. 2018, *Monthly Notices of the Royal Astronomical Society*, 473, 1258

Schulze, S., Yaron, O., Sollerman, J., et al. 2021, *ApJS*, 255, 29

Shahbandeh, M., Hsiao, E. Y., Ashall, C., et al. 2022, *ApJ*, 925, 175

Skrutskie, M. F., Cutri, R. M., Stiening, R., et al. 2006, *Astronomical Journal*, 131, 1163

Smartt, S. J. 2009, *ARA&A*, 47, 63

Smartt, S. J., Valenti, S., Fraser, M., et al. 2015, *Astronomy and Astrophysics*, 579, A40

Smith, N. 2017, *Interacting Supernovae: Types IIn and Ibn* (Springer), 403

Smith, N., Chornock, R., Silverman, J. M., Filippenko, A. V., & Foley, R. J. 2010, *The Astrophysical Journal*, 709, 856

Sollerman, J., Fransson, C., Barbarino, C., et al. 2020, *A&A*, 643, A79

Sukhbold, T., Ertl, T., Woosley, S. E., Brown, J. M., & Janka, H.-T. 2016, *ApJ*, 821, 38

Suwa, Y., Tominaga, N., & Maeda, K. 2019, *MNRAS*, 483, 3607

Taddia, F., Stritzinger, M. D., Bersten, M., et al. 2018, *A&A*, 609, A136

Taggart, K. & Perley, D. A. 2021, *MNRAS*, 503, 3931

Teffs, J., Ertl, T., Mazzali, P., Hachinger, S., & Janka, T. 2020, *MNRAS*, 492, 4369

Terraner, G., Pumo, M. L., Chen, T.-W., et al. 2017, *Nature Astronomy*, 1, 713

Tinyanont, S., Woosley, S. E., Taggart, K., et al. 2023, *ApJ*, 951, 34

Tody, D. 1986, in *Society of Photo-Optical Instrumentation Engineers (SPIE) Conference Series*, Vol. 627, *Instrumentation in astronomy VI*, ed. D. L. Crawford, 733

Tody, D. 1993, in *Astronomical Society of the Pacific Conference Series*, Vol. 52, *Astronomical Data Analysis Software and Systems II*, ed. R. J. Hanisch, R. J. V. Brissenden, & J. Barnes, 173

Tonry, J. L., Denneau, L., Flewelling, H., et al. 2018a, *ApJ*, 867, 105

Tonry, J. L., Denneau, L., Heinze, A. N., et al. 2018b, *PASP*, 130, 064505

Ugliano, M., Janka, H.-T., Marek, A., & Arcones, A. 2012, *ApJ*, 757, 69

Umeda, H. & Nomoto, K. 2008, *ApJ*, 673, 1014

van der Walt, S., Crellin-Quick, A., & Bloom, J. 2019, *The Journal of Open Source Software*, 4, 1247

van Dokkum, P. G. 2001, *PASP*, 113, 1420

West, S. L., Lunnan, R., Omand, C. M. B., et al. 2023, *A&A*, 670, A7

Wheeler, J. C., Chatzopoulos, E., Vinkó, J., & Tuminello, R. 2017, *ApJ*, 851, L14

Williamson, M., Kerzendorf, W., & Modjaz, M. 2021, *ApJ*, 908, 150

Wilson, J. C., Henderson, C. P., Herter, T. L., et al. 2004, in *Society of Photo-Optical Instrumentation Engineers (SPIE) Conference Series*, Vol. 5492, *Ground-based Instrumentation for Astronomy*, ed. A. F. M. Moorwood & M. Iye, 1295–1305

Winteler, C., Käppeli, R., Perego, A., et al. 2012, *ApJ*, 750, L22

Woosley, S. E. 2010, *ApJL*, 719, L204

Yan, L., Perley, D., Schulze, S., et al. 2020, *arXiv e-prints*, arXiv:2006.13758

Yaron, O. & Gal-Yam, A. 2012, *PASP*, 124, 668

Zhu, J., Jiang, N., Dong, S., et al. 2023, *ApJ*, 949, 23

<sup>1</sup> INAF - Osservatorio Astronomico d'Abruzzo, Via Mentore Maggini Snc, 64100 Teramo, Italy

<sup>2</sup> INAF - Osservatorio Astronomico di Padova, Vicoletto dell'Osservatorio 5, 35122 Padova, Italy

<sup>3</sup> Dipartimento di Fisica, "Sapienza" Università di Roma & Sezione INFN Roma1, Piazzale Aldo Moro 5, 00185 Roma, Italy

<sup>4</sup> Caltech Optical Observatories, California Institute of Technology, Pasadena, CA 91125, USA

<sup>5</sup> European Southern Observatory, Alonso de Córdova 3107, Casilla 19, Santiago, Chile

<sup>6</sup> National Research Center, Kurchatov Institute, pl. Kurchatova 1, Moscow 123182, Russia

<sup>7</sup> Lebedev Physical Institute, Russian Academy of Sciences, 53 Leninsky Avenue, Moscow 119991, Russia

<sup>8</sup> M.V. Lomonosov Moscow State University, Sternberg Astronomical Institute, 119234 Moscow, Russia

<sup>9</sup> Yunnan Observatories, Chinese Academy of Sciences, Kunming 650216, P.R. China

<sup>10</sup> International Centre of Supernovae, Yunnan Key Laboratory, Kunming 650216, P.R. China

<sup>11</sup> Graduate Institute of Astronomy, National Central University, 300 Jhongda Road, 32001 Jhongli, Taiwan

<sup>12</sup> Institute of Space Sciences (ICE, CSIC), Campus UAB, Carrer de Can Magrans, s/n, E-08193 Barcelona, Spain

<sup>13</sup> Department of Particle Physics and Astrophysics, Weizmann Institute of Science, Rehovot, Israel, 76100

<sup>14</sup> Division of Physics, Mathematics and Astronomy, California Institute of Technology, Pasadena, CA 91125, USA

<sup>15</sup> Astronomical Observatory, University of Warsaw, Al. Ujazdowskie 4, 00-478 Warszawa, Poland

<sup>16</sup> IPAC, California Institute of Technology, 1200 E. California Blvd, Pasadena, CA 91125, USA

<sup>17</sup> Institut d'Estudis Espacials de Catalunya (IEEC), Edifici RDIT, Campus UPC, 08860 Castelldefels (Barcelona), Spain

<sup>18</sup> Department of Astronomy, University of Florida, 211 Bryant Space Science Center, Gainesville, FL 32611-2055 USA

<sup>19</sup> Center for Astrophysics | Harvard & Smithsonian, 60 Garden Street, Cambridge, MA 02138-1516, USA

<sup>20</sup> The NSF AI Institute for Artificial Intelligence and Fundamental Interactions, USA

<sup>21</sup> Department of Physics, University of California, Santa Barbara, CA 93106-9530, USA

<sup>22</sup> Las Cumbres Observatory, 6740 Cortona Drive, Suite 102, Goleta, CA 93117-5575, USA

<sup>23</sup> Cardiff Hub for Astrophysics Research and Technology, School of Physics & Astronomy, Cardiff University, Queens Buildings, The Parade, Cardiff, CF24 3AA, UK

<sup>24</sup> HUN-REN Research Centre for Astronomy and Earth Sciences, Konkoly Observatory, MTA Centre of Excellence, Konkoly Thege Miklós út 15-17., H-1121 Budapest, Hungary

<sup>25</sup> Department of Experimental Physics, Institute of Physics, University of Szeged, Dóm tér 9, Szeged, 6720 Hungary

<sup>26</sup> The Oskar Klein Centre, Department of Astronomy, AlbaNova, Stockholm University, SE-106 91 Stockholm, Sweden

<sup>27</sup> School of Physics and Astronomy, University of Leicester, University Road, Leicester LE1 7RH, UK

<sup>28</sup> School of Physics, Trinity College Dublin, The University of Dublin, Dublin 2, Ireland

<sup>29</sup> Instituto de Ciencias Exactas y Naturales (ICEN), Universidad Arturo Prat, Chile

<sup>30</sup> University of Texas at Austin, 1 University Station C1400, Austin, TX 78712-0259, USA

<sup>31</sup> Astrophysics Research Centre, School of Mathematics and Physics, Queen's University Belfast, Belfast BT7 1NN, UK

<sup>32</sup> Department of Physics and Astronomy, University of Padova, Via F. Marzolo 8, I-35131 Padova, Italy

<sup>33</sup> Johns Hopkins University Bloomberg Center for Physics and Astronomy San Martin Dr, Baltimore, MD 21210

<sup>34</sup> Instituto de Alta Investigación, Universidad de Tarapacá, Casilla 7D, Arica, Chile

<sup>35</sup> Dipartimento di Fisica "Ettore Pancini", Università di Napoli Federico II, Via Cinthia 9, 80126 Naples, Italy

<sup>36</sup> INAF - Osservatorio Astronomico di Capodimonte, Salita Moiariello 16, 80131 Napoli, Italy

<sup>37</sup> INAF - Osservatorio Astronomico di Brera, Via Bianchi 46, 23807 Merate (LC), Italy

<sup>38</sup> Tuorla Observatory, Department of Physics and Astronomy, University of Turku, FI-20014 Turku, Finland

<sup>39</sup> Cosmic Dawn Center (DAWN)

<sup>40</sup> Niels Bohr Institute, University of Copenhagen, Jagtvej 128, 2200 København N, Denmark

<sup>41</sup> Center for Interdisciplinary Exploration and Research in Astrophysics (CIERA), Northwestern University, 1800 Sherman Ave., Evanston, IL 60201, USA

<sup>42</sup> School of Physics and Astronomy, University of Minnesota, Minneapolis, MN55455, USA

<sup>43</sup> Henan Academy of Sciences, Zhengzhou 450046, Henan, China

## Appendix A: Observations and data reduction

### Appendix A.1: Photometry

Optical/NIR photometry of SN 2021bnw was obtained exploiting several observational facilities: *i*) New Technology Telescope (NTT) with the EFOSC2 (ESO Faint Object Spectrograph and Camera, Buzzoni et al. 1984) and SOFI (Son of ISAAC, Moorwood et al. 1998) Camera, La Silla Observatory, Chile via ePESSTO+; *ii*) the 2.56m Nordic Optical Telescope (NOT) via the NOT Unbiased Transient Survey (NUTS2, Holmbo et al. 2019) + the Alhambra Faint Object Spectrograph and Camera (ALFOSC), La Palma Observatory, Spain; *iii*) with the camera Sinistro built for the 1-m class telescopes of the Las Cumbres Observatory<sup>4</sup> (LCO) telescope network under the Global Supernova Project (GSP) collaboration; *iv*) the 1.82m Copernico+AFOSC and Schmidt telescopes operated by INAF Osservatorio Astronomico di Padova at Asiago-Cima Ekar. In addition, we used the ATLAS (Asteroid Terrestrial-impact Last Alert System, Tonry et al. 2018a,b) *o*-, *c*-filters photometry and the ZTF *g*- and *r*-filters photometry. ZTF uses the Samuel Oschin 48-inch (1.22 m) Schmidt telescope at Palomar Observatory on Mount Palomar (USA), utilizing the Fritz Marshal System (van der Walt et al. 2019; Coughlin et al. 2023). The Samuel Oschin Schmidt telescope is equipped with a 47-square-degree camera (Dekany et al. 2020) and monitors the entire northern hemisphere every 2–3 days in the *g* and *r* bands to a depth of  $\sim 20.7$  mag ( $5\sigma$ ; Bellm et al. 2019b; Graham et al. 2019) as part of the public ZTF Northern Sky Survey (Bellm et al. 2019a). We retrieved the host-subtracted photometry via the Infrared Processing and Analysis Center ZTF forced-photometry service (Masci et al. 2023). This service uses the data-reduction techniques outlined in Masci et al. (2019). We cleaned and calibrated the data following Masci et al. (2023).

We performed magnitude measurements with the `ecsnoopy` package<sup>5</sup> (Cappellaro 2014). Background contamination was removed from the SN light by performing template subtraction with the `hotpants` tool (Becker 2015). *u*-, *g*-, *r*-, *i*-, *z*-filters templates were obtained via the Sloan Digital Sky Survey (SDSS) and *B*-, *V*-filter templates were observed at the NOT telescope on 2023 May 5, i.e. 833 days after maximum. We assume that at this epoch SN 2021bnw faded well below the detection limit. *J*-, *H*-, *K*-filter templates were obtained via the Two Micron All Sky Survey (2MASS, Skrutskie et al. 2006). Then, we calibrated the instrumental *u*-, *g*-, *r*-, *i*-, *z*- and *J*-, *H*-, *K*-filters magnitudes against a series of non-saturated field stars present in the Pan-STARRS (Panoramic Survey Telescope and Rapid Response System Chambers et al. 2016) and the 2MASS catalogs, respectively, while the *B*-, *V*-filters magnitudes were calibrated following the color transformations of Chonis & Gaskell (2008). The reduced optical and NIR photometry is listed in Tables B.1, B.2.

### Appendix A.2: Spectroscopy

We obtained optical spectroscopy of SN 2021bnw at NTT+EFOSC2 via ePESSTO+, at NOT+ALFOSC via NUTS2, at 1.82m Copernico+AFOSC at INAF, Osservatorio Astronomico di Padova at Asiago-Cima Ekar and LCO 1.0m telescopes+Sinistro and at the Palomar 60-inch telescope+SEDM (Spectral Energy Distribution Machine, Blagorodnova et al. 2018). We also obtained a NIR spectrum at 87 days after maximum luminosity at Keck+NIRES (Near-Infrared Echelle Spectrometer, Wilson et al. 2004). The log of the spectroscopic observations is shown in Table B.3.

Raw optical NTT+EFOSC2 spectroscopic frames were initially corrected for overscan, bias and flat field. Then the extracted trace was calibrated in wavelength with HeAr (for the NTT+EFOSC2), HeNe (for NOT+ALFOSC spectra), NeHgCd (for the 1.82m- Copernico+AFOSC spectra) lamps and in flux using the spectrum of a spectrophotometric standard star observed on the same night and with the same instrumental set-up of each scientific observation. Moreover, we account for the cosmic-ray contamination with the python package `lacosmic`<sup>6</sup>, based on the Laplacian edge detection (L. A. Cosmic) algorithm by van Dokkum (2001). NTT+EFOSC2 spectra were processed with IRAF (Image Reduction and Analysis Facility, Tody 1986, 1993). For Asiago and NOT spectra, the same procedures were called via the graphical user interface `foscgui`<sup>7</sup>. SEDM spectra are reduced with the tool `pysedm` (Rigault et al. 2019).

## Appendix B: Tables

<sup>4</sup> <http://lco.global>

<sup>5</sup> `ecsnoopy` is a python package for SN photometry using PSF fitting and template subtraction developed by E. Cappellaro. A package description can be found at <http://sngroup.oapd.inaf.it/>.

<sup>6</sup> <https://lacosmic.readthedocs.io/>.

<sup>7</sup> `foscgui` is a python/pyraf based graphic user interface aimed at extracting SN spectroscopy and photometry obtained with FOSC-like instruments. It was developed by E. Cappellaro. A package description can be found at <http://sngroup.oapd.inaf.it/foscgui.html>.

**Table B.1.** (Non  $K$ -corrected) optical magnitudes measurements for SN 2021bnw expressed in AB mag. The errors are expressed in parenthesis. Numbers with asterisk correspond to detection limits.

| MJD      | $u$         | $B$         | $g$         | $V$         | $r$         | $i$         | instrument | $\log_{10} L_{\text{bol}}$ |
|----------|-------------|-------------|-------------|-------------|-------------|-------------|------------|----------------------------|
| 59219.44 | -           | -           | 19.69*      | -           | -           | -           | ZTF        | -                          |
| 59219.48 | -           | -           | -           | -           | 19.82*      | -           | ZTF        | -                          |
| 59221.45 | -           | -           | -           | -           | 20.07*      | -           | ZTF        | -                          |
| 59221.46 | -           | -           | 19.11*      | -           | -           | -           | ZTF        | -                          |
| 59223.38 | -           | -           | 20.38*      | -           | -           | -           | ZTF        | -                          |
| 59223.46 | -           | -           | -           | -           | 20.07*      | -           | ZTF        | -                          |
| 59225.41 | -           | -           | -           | -           | 20.09*      | -           | ZTF        | -                          |
| 59225.44 | -           | -           | 20.0*       | -           | -           | -           | ZTF        | -                          |
| 59227.44 | -           | -           | 21.07(0.41) | -           | -           | -           | ZTF        | 42.27(0.04)                |
| 59231.42 | -           | -           | 20.49(0.27) | -           | -           | -           | ZTF        | 42.51(0.03)                |
| 59248.41 | -           | -           | 17.97(0.06) | -           | -           | -           | ZTF        | 43.54(0.03)                |
| 59250.37 | -           | -           | 17.86(0.06) | -           | -           | -           | ZTF        | 43.58(0.03)                |
| 59250.38 | -           | -           | -           | -           | 18.11(0.07) | -           | ZTF        | -                          |
| 59252.32 | -           | -           | -           | -           | 17.93(0.06) | -           | ZTF        | -                          |
| 59252.38 | -           | -           | 17.71(0.06) | -           | -           | -           | ZTF        | 43.64(0.02)                |
| 59254.14 | -           | 17.76(0.01) | -           | -           | -           | -           | Sinistro   | -                          |
| 59254.15 | -           | -           | -           | 17.7(0.01)  | -           | -           | Sinistro   | 43.60(0.02)                |
| 59254.16 | -           | -           | 17.85(0.02) | -           | 17.81(0.01) | -           | Sinistro   | -                          |
| 59254.17 | -           | -           | -           | -           | -           | 17.83(0.02) | Sinistro   | -                          |
| 59254.30 | -           | -           | 17.62(0.06) | -           | -           | -           | ZTF        | 43.66(0.02)                |
| 59256.37 | -           | -           | 17.52(0.05) | -           | -           | -           | ZTF        | 43.69(0.02)                |
| 59256.40 | -           | -           | -           | -           | 17.74(0.04) | -           | ZTF        | -                          |
| 59258.14 | -           | 17.62(0.01) | -           | 17.55(0.02) | -           | -           | Sinistro   | -                          |
| 59258.34 | -           | -           | -           | -           | 17.67(0.05) | -           | ZTF        | -                          |
| 59258.37 | -           | -           | 17.45(0.05) | -           | -           | -           | ZTF        | 43.71(0.02)                |
| 59260.90 | 17.31(0.03) | -           | -           | -           | -           | -           | Schmidt    | -                          |
| 59260.91 | -           | 17.39(0.02) | -           | -           | -           | -           | Schmidt    | -                          |
| 59260.92 | -           | -           | -           | 17.42(0.02) | -           | -           | Schmidt    | -                          |
| 59260.93 | -           | -           | 17.34(0.01) | -           | -           | -           | Schmidt    | 43.76(0.02)                |
| 59260.94 | -           | -           | -           | -           | 17.59(0.02) | 17.76(0.02) | Schmidt    | -                          |
| 59262.23 | -           | 17.52(0.01) | -           | -           | -           | -           | Sinistro   | -                          |
| 59262.24 | -           | -           | -           | 17.43(0.01) | -           | -           | Sinistro   | -                          |
| 59262.25 | -           | -           | -           | -           | 17.58(0.01) | -           | Sinistro   | -                          |
| 59262.26 | -           | -           | -           | -           | -           | 17.53(0.02) | Sinistro   | -                          |
| 59262.35 | -           | -           | -           | -           | 17.57(0.05) | -           | ZTF        | -                          |
| 59262.41 | -           | -           | 17.39(0.06) | -           | -           | -           | ZTF        | 43.76(0.02)                |
| 59264.36 | -           | -           | -           | -           | 17.55(0.04) | -           | ZTF        | -                          |
| 59265.30 | -           | 17.56(0.02) | -           | -           | -           | -           | Sinistro   | -                          |
| 59265.31 | -           | -           | -           | 17.46(0.02) | -           | -           | Sinistro   | -                          |
| 59265.32 | -           | -           | 17.63(0.01) | -           | -           | -           | Sinistro   | 43.73(0.02)                |
| 59265.33 | -           | -           | -           | -           | 17.53(0.04) | 17.53(0.03) | Sinistro   | -                          |
| 59266.33 | -           | -           | -           | -           | 17.6(0.06)  | -           | ZTF        | -                          |
| 59266.42 | -           | -           | 17.45(0.06) | -           | -           | -           | ZTF        | 43.74(0.03)                |
| 59267.82 | 17.42(0.09) | -           | -           | -           | -           | -           | Schmidt    | -                          |
| 59267.83 | -           | 17.48(0.06) | -           | -           | -           | -           | Schmidt    | -                          |
| 59267.84 | -           | -           | 17.37(0.04) | 17.45(0.05) | -           | -           | Schmidt    | 43.74(0.03)                |
| 59267.85 | -           | -           | -           | -           | 17.57(0.04) | -           | Schmidt    | -                          |
| 59267.86 | -           | -           | -           | -           | -           | 17.63(0.06) | Schmidt    | -                          |
| 59268.35 | -           | -           | -           | -           | 17.58(0.04) | -           | ZTF        | -                          |
| 59268.43 | -           | -           | 17.43(0.05) | -           | -           | -           | ZTF        | 43.73(0.03)                |
| 59270.31 | -           | -           | -           | -           | 17.56(0.05) | -           | ZTF        | -                          |
| 59270.38 | -           | -           | 17.48(0.06) | -           | -           | -           | ZTF        | 43.72(0.03)                |
| 59270.94 | -           | -           | 17.76(0.09) | -           | -           | -           | Sinistro   | 43.70(0.03)                |
| 59271.03 | -           | 17.61(0.07) | -           | -           | -           | -           | Schmidt    | -                          |
| 59273.82 | 17.61(0.04) | -           | -           | -           | -           | -           | Schmidt    | -                          |
| 59273.83 | -           | 17.55(0.03) | -           | -           | -           | -           | Schmidt    | -                          |
| 59273.84 | -           | -           | -           | 17.52(0.03) | -           | -           | Schmidt    | -                          |
| 59273.85 | -           | -           | 17.43(0.03) | -           | 17.65(0.03) | -           | Schmidt    | 43.71(0.03)                |
| 59273.86 | -           | -           | -           | -           | -           | 17.68(0.03) | Schmidt    | -                          |

**Table B.1.** continued.

| MJD      | <i>u</i>    | <i>B</i>    | <i>g</i>    | <i>V</i>    | <i>r</i>    | <i>i</i>    | instrument | $\log_{10} L_{\text{bol}}$ |
|----------|-------------|-------------|-------------|-------------|-------------|-------------|------------|----------------------------|
| 59274.24 | -           | -           | 17.5(0.1)   | -           | -           | -           | ZTF        | 43.70(0.03)                |
| 59274.36 | -           | -           | -           | -           | 17.61(0.07) | -           | ZTF        | -                          |
| 59274.69 | -           | 17.66(0.11) | -           | -           | -           | -           | Sinistro   | -                          |
| 59274.70 | -           | -           | 17.52*      | 17.55(0.17) | -           | -           | Sinistro   | -                          |
| 59274.92 | -           | -           | -           | -           | 17.6(0.02)  | 17.7(0.02)  | Schmidt    | -                          |
| 59274.93 | -           | -           | 17.48(0.02) | -           | -           | -           | Schmidt    | 43.71(0.03)                |
| 59274.94 | -           | -           | -           | 17.55(0.03) | -           | -           | Schmidt    | -                          |
| 59274.95 | 17.48(0.03) | 17.7(0.09)  | -           | -           | -           | -           | Schmidt    | -                          |
| 59276.26 | -           | -           | 17.56(0.06) | -           | -           | -           | ZTF        | 43.69(0.03)                |
| 59276.34 | -           | -           | -           | -           | 17.62(0.05) | -           | ZTF        | -                          |
| 59276.93 | -           | 17.73(0.1)  | -           | -           | -           | -           | Schmidt    | -                          |
| 59276.94 | 17.58(0.1)  | -           | -           | -           | -           | -           | Schmidt    | -                          |
| 59278.83 | -           | 17.73(0.01) | -           | 17.59(0.01) | -           | -           | Sinistro   | 43.68(0.03)                |
| 59278.84 | -           | -           | 17.58(0.01) | -           | 17.65(0.01) | 17.7(0.02)  | Sinistro   | -                          |
| 59279.88 | -           | 17.64(0.02) | -           | -           | -           | -           | Schmidt    | -                          |
| 59280.29 | -           | -           | -           | -           | 17.67(0.05) | -           | ZTF        | -                          |
| 59280.36 | -           | -           | 17.64(0.07) | -           | -           | -           | ZTF        | 43.67(0.03)                |
| 59285.79 | -           | -           | -           | -           | 17.69(0.05) | -           | Schmidt    | -                          |
| 59285.80 | -           | -           | -           | -           | -           | 17.87(0.07) | Schmidt    | -                          |
| 59285.81 | -           | -           | 17.8(0.04)  | -           | -           | -           | Schmidt    | 43.63(0.04)                |
| 59285.82 | -           | 17.61(0.08) | -           | 17.74(0.04) | -           | -           | Schmidt    | -                          |
| 59285.83 | 17.92(0.09) | -           | -           | -           | -           | -           | Schmidt    | -                          |
| 59286.00 | -           | 17.84(0.01) | -           | -           | -           | -           | Sinistro   | -                          |
| 59286.01 | -           | -           | -           | 17.67(0.01) | -           | -           | Sinistro   | -                          |
| 59290.21 | -           | 17.87(0.01) | -           | 17.74(0.01) | -           | -           | Sinistro   | -                          |
| 59290.22 | -           | -           | 17.65(0.02) | -           | 17.73(0.03) | -           | Sinistro   | 43.63(0.03)                |
| 59290.23 | -           | -           | -           | -           | -           | 17.67(0.02) | Sinistro   | -                          |
| 59290.26 | -           | -           | -           | -           | 17.76(0.06) | -           | ZTF        | -                          |
| 59290.30 | -           | -           | 17.73(0.08) | -           | -           | -           | ZTF        | 43.62(0.04)                |
| 59290.78 | -           | -           | -           | -           | 17.79(0.02) | -           | Schmidt    | -                          |
| 59290.79 | -           | -           | -           | -           | -           | 17.84(0.02) | Schmidt    | -                          |
| 59290.80 | -           | -           | 17.69(0.02) | 17.7(0.02)  | -           | -           | Schmidt    | 43.62(0.03)                |
| 59290.81 | -           | 17.75(0.03) | -           | -           | -           | -           | Schmidt    | -                          |
| 59290.82 | 18.07(0.22) | -           | -           | -           | -           | -           | Schmidt    | -                          |
| 59291.89 | 17.99(0.03) | -           | -           | -           | -           | -           | ALFOSC     | -                          |
| 59291.90 | -           | 17.87(0.06) | -           | 17.68(0.05) | -           | 17.8(0.03)  | ALFOSC     | -                          |
| 59292.25 | -           | -           | -           | -           | 17.77(0.05) | -           | ZTF        | -                          |
| 59292.29 | -           | -           | 17.73(0.07) | -           | -           | -           | ZTF        | 43.62(0.02)                |
| 59294.20 | -           | 17.95(0.01) | -           | 17.76(0.01) | -           | -           | Sinistro   | -                          |
| 59294.21 | -           | -           | 18.0(0.02)  | -           | 17.77(0.01) | -           | Sinistro   | 43.60(0.02)                |
| 59294.22 | -           | -           | -           | -           | -           | 17.74(0.02) | Sinistro   | -                          |
| 59294.25 | -           | -           | 17.77(0.07) | -           | -           | -           | ZTF        | 43.61(0.02)                |
| 59294.32 | -           | -           | -           | -           | 17.77(0.05) | -           | ZTF        | -                          |
| 59295.78 | -           | -           | -           | -           | 17.86(0.03) | 17.85(0.03) | Schmidt    | -                          |
| 59295.79 | -           | -           | 17.71(0.02) | -           | -           | -           | Schmidt    | 43.61(0.02)                |
| 59295.80 | -           | -           | -           | 17.73(0.03) | -           | -           | Schmidt    | -                          |
| 59295.81 | -           | 17.75(0.03) | -           | -           | -           | -           | Schmidt    | -                          |
| 59297.21 | -           | -           | 17.77(0.09) | -           | -           | -           | ZTF        | -                          |
| 59297.26 | -           | -           | -           | -           | 17.81(0.05) | -           | ZTF        | -                          |
| 59298.13 | -           | 17.9(0.02)  | -           | 17.77(0.02) | -           | -           | Sinistro   | -                          |
| 59298.14 | -           | -           | 17.73(0.01) | -           | 17.84(0.02) | -           | Sinistro   | 43.61(0.02)                |
| 59298.15 | -           | -           | -           | -           | -           | 17.76(0.02) | Sinistro   | -                          |
| 59301.36 | -           | -           | -           | -           | 17.73(0.09) | -           | ZTF        | -                          |
| 59302.26 | -           | 17.92(0.03) | -           | -           | -           | -           | Sinistro   | -                          |
| 59302.27 | -           | -           | 17.77(0.03) | 17.73(0.03) | -           | -           | Sinistro   | 43.59(0.02)                |
| 59303.28 | -           | -           | 17.83(0.07) | -           | -           | -           | ZTF        | 43.59(0.02)                |
| 59303.35 | -           | -           | -           | -           | 17.77(0.06) | -           | ZTF        | -                          |
| 59305.29 | -           | -           | 17.85(0.07) | -           | -           | -           | ZTF        | 43.58(0.02)                |
| 59305.85 | -           | -           | -           | -           | 17.87(0.01) | -           | Schmidt    | -                          |
| 59305.86 | -           | -           | -           | -           | -           | 17.95(0.02) | Schmidt    | -                          |
| 59305.87 | -           | -           | 17.8(0.01)  | 17.83(0.03) | -           | -           | Schmidt    | 43.58(0.02)                |

**Table B.1.** continued.

| MJD      | <i>u</i>    | <i>B</i>    | <i>g</i>    | <i>V</i>    | <i>r</i>    | <i>i</i>    | instrument | $\log_{10} L_{\text{bol}}$ |
|----------|-------------|-------------|-------------|-------------|-------------|-------------|------------|----------------------------|
| 59305.88 | -           | 17.97(0.08) | -           | -           | -           | -           | Schmidt    | -                          |
| 59305.89 | 18.16(0.04) | -           | -           | -           | -           | -           | Schmidt    | -                          |
| 59306.05 | -           | 18.03(0.01) | -           | -           | -           | -           | Sinistro   | -                          |
| 59306.07 | -           | -           | 17.8(0.01)  | 17.83(0.02) | -           | -           | Sinistro   | 43.59(0.01)                |
| 59306.08 | -           | -           | -           | -           | 17.88(0.01) | 17.77(0.01) | Sinistro   | -                          |
| 59307.25 | -           | -           | -           | -           | 17.84(0.06) | -           | ZTF        | -                          |
| 59307.28 | -           | -           | 17.87(0.06) | -           | -           | -           | ZTF        | 43.57(0.02)                |
| 59309.19 | -           | -           | 17.96(0.05) | -           | -           | -           | ZTF        | 43.54(0.02)                |
| 59309.23 | -           | -           | -           | -           | 17.96(0.05) | -           | ZTF        | -                          |
| 59310.89 | -           | -           | -           | -           | 17.98(0.03) | -           | Schmidt    | -                          |
| 59310.90 | -           | -           | -           | -           | -           | 18.07(0.04) | Schmidt    | -                          |
| 59310.91 | -           | -           | 17.94(0.02) | 17.93(0.02) | -           | -           | Schmidt    | 43.52(0.02)                |
| 59310.92 | -           | 18.11(0.03) | -           | -           | -           | -           | Schmidt    | -                          |
| 59310.93 | 18.46(0.06) | -           | -           | -           | -           | -           | Schmidt    | -                          |
| 59311.17 | -           | -           | -           | -           | 17.93(0.06) | -           | ZTF        | -                          |
| 59311.21 | -           | -           | 17.98(0.1)  | -           | -           | -           | ZTF        | 43.52(0.02)                |
| 59311.84 | -           | 18.22(0.01) | -           | -           | -           | -           | Sinistro   | -                          |
| 59311.85 | -           | -           | 18.0(0.01)  | 17.96(0.01) | -           | -           | Sinistro   | 43.51(0.02)                |
| 59311.86 | -           | -           | -           | -           | 17.97(0.01) | 18.06(0.03) | Sinistro   | -                          |
| 59313.21 | -           | -           | -           | -           | 18.02(0.06) | -           | ZTF        | -                          |
| 59313.23 | -           | -           | 18.08(0.09) | -           | -           | -           | ZTF        | 43.50(0.02)                |
| 59313.95 | -           | -           | -           | -           | 18.08(0.02) | -           | Schmidt    | -                          |
| 59313.96 | -           | -           | -           | -           | -           | 18.09(0.03) | Schmidt    | 43.49(0.02)                |
| 59313.97 | -           | -           | 18.05(0.02) | 18.02(0.02) | -           | -           | Schmidt    | -                          |
| 59313.98 | -           | 18.26(0.04) | -           | -           | -           | -           | Schmidt    | -                          |
| 59315.21 | -           | -           | 18.16(0.07) | -           | -           | -           | ZTF        | 43.48(0.02)                |
| 59315.80 | -           | 18.39(0.01) | -           | 18.06(0.01) | -           | -           | Sinistro   | -                          |
| 59315.81 | -           | -           | 18.09(0.01) | -           | 18.07(0.02) | -           | Sinistro   | 43.48(0.02)                |
| 59315.82 | -           | -           | -           | -           | -           | 18.06(0.02) | Sinistro   | -                          |
| 59317.19 | -           | -           | -           | -           | 18.11(0.04) | -           | ZTF        | -                          |
| 59317.23 | -           | -           | 18.21(0.09) | -           | -           | -           | ZTF        | 43.46(0.02)                |
| 59320.17 | -           | -           | 18.28(0.07) | -           | -           | -           | ZTF        | 43.44(0.02)                |
| 59320.81 | -           | 18.71(0.02) | -           | 18.2(0.02)  | -           | -           | Sinistro   | -                          |
| 59320.82 | -           | -           | 18.24(0.01) | -           | -           | -           | Sinistro   | 43.44(0.02)                |
| 59322.27 | -           | -           | -           | -           | 18.12(0.06) | -           | ZTF        | -                          |
| 59324.17 | -           | -           | 18.29(0.11) | -           | -           | -           | ZTF        | 43.43(0.02)                |
| 59324.21 | -           | -           | -           | -           | 18.08(0.06) | -           | ZTF        | -                          |
| 59329.23 | -           | -           | -           | -           | 18.1(0.07)  | -           | ZTF        | -                          |
| 59329.31 | -           | -           | 18.15(0.11) | -           | -           | -           | ZTF        | 43.44(0.03)                |
| 59331.15 | -           | 18.66(0.1)  | -           | -           | -           | -           | Sinistro   | 43.42(0.03)                |
| 59331.16 | -           | -           | 18.24(0.06) | -           | -           | -           | Sinistro   | -                          |
| 59335.19 | -           | -           | -           | -           | 18.17(0.06) | -           | ZTF        | -                          |
| 59335.21 | -           | -           | 18.38(0.11) | -           | -           | -           | ZTF        | 43.40(0.03)                |
| 59337.94 | -           | -           | -           | -           | 18.25(0.02) | 18.16(0.03) | Schmidt    | -                          |
| 59337.95 | -           | -           | 18.39(0.02) | -           | -           | -           | Schmidt    | 43.39(0.03)                |
| 59337.96 | -           | 18.52(0.04) | -           | 18.3(0.03)  | -           | -           | Schmidt    | -                          |
| 59337.97 | 18.94(0.13) | -           | -           | -           | -           | -           | Schmidt    | -                          |
| 59338.19 | -           | -           | 18.43(0.09) | -           | -           | -           | ZTF        | 43.39(0.03)                |
| 59338.24 | -           | -           | -           | -           | 18.19(0.06) | -           | ZTF        | -                          |
| 59340.19 | -           | -           | 18.39(0.09) | -           | -           | -           | ZTF        | 43.39(0.03)                |
| 59340.23 | -           | -           | -           | -           | 18.23(0.06) | -           | ZTF        | -                          |
| 59342.24 | -           | -           | 18.47(0.08) | -           | -           | -           | ZTF        | -                          |
| 59342.29 | -           | -           | -           | -           | 18.22(0.08) | -           | ZTF        | -                          |
| 59344.04 | -           | -           | 18.75(0.03) | 18.18(0.12) | -           | -           | Sinistro   | 43.33(0.03)                |
| 59344.05 | -           | -           | -           | -           | 18.29(0.06) | 18.24(0.09) | Sinistro   | -                          |
| 59344.21 | -           | -           | -           | -           | 18.28(0.06) | -           | ZTF        | -                          |
| 59344.27 | -           | -           | 18.43(0.08) | -           | -           | -           | ZTF        | 43.36(0.03)                |
| 59346.33 | -           | -           | 18.46(0.12) | -           | -           | -           | ZTF        | 43.35(0.03)                |
| 59348.18 | -           | -           | -           | -           | 18.31(0.07) | -           | ZTF        | -                          |
| 59348.93 | 4.59*       | -           | -           | -           | -           | -           | ALFOSC     | -                          |
| 59350.08 | -           | 18.76(0.02) | -           | -           | -           | -           | Sinistro   | -                          |

**Table B.1.** continued.

| MJD      | <i>u</i>    | <i>B</i>   | <i>g</i>    | <i>V</i>    | <i>r</i>    | <i>i</i>    | instrument | $\log_{10} L_{\text{bol}}$ |
|----------|-------------|------------|-------------|-------------|-------------|-------------|------------|----------------------------|
| 59350.09 | -           | -          | 18.49(0.01) | 18.34*      | -           | -           | Sinistro   | 43.33(0.02)                |
| 59350.10 | -           | -          | -           | -           | 18.4(0.03)  | 18.25(0.03) | Sinistro   | -                          |
| 59350.18 | -           | -          | 18.55(0.11) | -           | -           | -           | ZTF        | 43.32(0.03)                |
| 59350.23 | -           | -          | -           | -           | 18.34(0.07) | -           | ZTF        | -                          |
| 59351.89 | -           | -          | -           | -           | 18.44(0.03) | -           | Schmidt    | -                          |
| 59351.90 | -           | -          | -           | -           | -           | 18.36(0.04) | Schmidt    | -                          |
| 59351.91 | -           | -          | 18.5(0.02)  | -           | -           | -           | Schmidt    | 43.31(0.03)                |
| 59351.92 | 19.53(0.16) | 18.8(0.05) | -           | 18.44(0.03) | -           | -           | Schmidt    | -                          |
| 59351.93 | -           | -          | -           | -           | -           | -           | Schmidt    | -                          |
| 59353.19 | -           | -          | -           | -           | 18.36(0.08) | -           | ZTF        | -                          |
| 59353.22 | -           | -          | 18.59(0.13) | -           | -           | -           | ZTF        | 43.29(0.03)                |
| 59356.24 | -           | -          | -           | -           | 18.46(0.11) | -           | ZTF        | -                          |
| 59357.05 | -           | 18.43*     | -           | -           | -           | -           | Sinistro   | -                          |
| 59357.06 | -           | -          | 18.84(0.05) | 18.3*       | -           | -           | Sinistro   | 43.21(0.03)                |
| 59357.07 | -           | -          | -           | -           | 18.34*      | -           | Sinistro   | -                          |
| 59358.26 | -           | -          | 18.78(0.21) | -           | -           | -           | ZTF        | 43.20(0.04)                |
| 59360.90 | -           | -          | -           | -           | 18.83(0.1)  | -           | Schmidt    | -                          |
| 59361.19 | -           | -          | -           | -           | 18.71(0.09) | -           | ZTF        | -                          |
| 59361.26 | -           | -          | 19.02(0.26) | -           | -           | -           | ZTF        | 43.15(0.04)                |
| 59361.86 | -           | -          | -           | -           | 18.73(0.04) | -           | Schmidt    | -                          |
| 59361.87 | -           | -          | -           | -           | -           | 18.83(0.07) | Schmidt    | -                          |
| 59361.88 | -           | -          | 18.91(0.05) | 18.9(0.07)  | -           | -           | Schmidt    | 43.15(0.04)                |
| 59361.89 | 19.13(0.09) | -          | -           | -           | -           | -           | Schmidt    | -                          |
| 59363.06 | 19.45(0.06) | -          | -           | -           | -           | -           | Sinistro   | -                          |
| 59363.07 | -           | -          | -           | 18.95(0.05) | -           | -           | Sinistro   | -                          |
| 59363.08 | -           | -          | -           | -           | 18.87(0.04) | 18.7(0.04)  | Sinistro   | -                          |
| 59363.21 | -           | -          | 19.07(0.12) | -           | -           | -           | ZTF        | 43.11(0.03)                |
| 59365.18 | -           | -          | -           | -           | 18.89(0.09) | -           | ZTF        | -                          |
| 59365.21 | -           | -          | 19.26(0.15) | -           | -           | -           | ZTF        | -                          |
| 59367.21 | -           | -          | -           | -           | 19.06(0.09) | -           | ZTF        | -                          |
| 59367.23 | -           | -          | 19.5(0.17)  | -           | -           | -           | ZTF        | 43.00(0.04)                |
| 59368.97 | 19.82(0.03) | -          | -           | 19.16(0.04) | -           | -           | Sinistro   | -                          |
| 59368.98 | -           | -          | 19.68(0.02) | -           | 19.17(0.04) | -           | Sinistro   | 42.95(0.04)                |
| 59368.99 | -           | -          | -           | -           | -           | 19.04(0.04) | Sinistro   | -                          |
| 59369.22 | -           | -          | 19.56(0.17) | -           | -           | -           | ZTF        | 42.96(0.04)                |
| 59371.23 | -           | -          | -           | -           | 19.31(0.12) | -           | ZTF        | -                          |
| 59373.22 | -           | -          | -           | -           | 19.32(0.12) | -           | ZTF        | -                          |
| 59374.91 | -           | -          | 135.56*     | -           | -           | -           | ALFOSC     | -                          |
| 59375.23 | -           | -          | -           | -           | 19.36(0.15) | -           | ZTF        | -                          |
| 59379.39 | 20.15(0.04) | -          | -           | -           | -           | -           | Sinistro   | -                          |
| 59379.40 | -           | -          | 19.74(0.03) | 19.58(0.04) | -           | -           | Sinistro   | 42.86(0.04)                |
| 59379.41 | -           | -          | -           | -           | 19.43(0.03) | 19.3(0.06)  | Sinistro   | -                          |
| 59389.97 | -           | -          | 22.67(0.72) | -           | -           | -           | Sinistro   | 42.45(0.06)                |
| 59398.97 | 21.67(0.56) | 21.05*     | -           | -           | -           | -           | Sinistro   | -                          |
| 59398.98 | -           | -          | -           | -           | -           | 16.78*      | Sinistro   | -                          |
| 59583.24 | -           | -          | -           | -           | 23.0*       | -           | ALFOSC     | -                          |
| 59583.25 | -           | -          | -           | -           | -           | 22.59(0.12) | ALFOSC     | -                          |
| 59583.24 | -           | -          | -           | -           | 23.0*       | -           | ALFOSC     | -                          |
| 59583.25 | -           | -          | -           | -           | -           | 22.59(0.12) | ALFOSC     | -                          |

**Table B.2.** (Non  $K$ -corrected)  $z$ ,  $J$ ,  $H$ ,  $K$  magnitudes measurements (error are in parenthesis, asterisks denote detection limits).

| MJD      | $z$    | $J$         | $H$         | $K$         | instrument |
|----------|--------|-------------|-------------|-------------|------------|
| 59264.08 | -      | 17.27(0.25) | -           | -           | NOTCAM     |
| 59264.09 | -      | -           | -           | 16.69(0.29) | NOTCAM     |
| 59278.23 | -      | 17.42(0.43) | -           | -           | SOFI       |
| 59278.24 | -      | -           | -           | 17.81*      | SOFI       |
| 59278.26 | -      | -           | 15.92(0.46) | -           | SOFI       |
| 59291.90 | 17.01* | -           | -           | -           | ALFOSC     |
| 59308.07 | -      | 17.26(0.03) | -           | -           | SOFI       |
| 59308.09 | -      | -           | -           | 16.74*      | SOFI       |
| 59308.11 | -      | -           | 16.0(0.33)  | -           | SOFI       |
| 59315.00 | -      | 17.18(0.18) | -           | -           | SOFI       |
| 59315.02 | -      | -           | -           | 17.0*       | SOFI       |
| 59315.03 | -      | -           | 16.23(0.06) | -           | SOFI       |

**Table B.3.** Log of the spectroscopic observations and  $K$  corrections in  $B$ ,  $g$ ,  $V$ ,  $r$ ,  $i$  filters computed on each spectrum.

| MJD      | Instrumental set up | Resolution[Å] | $K_B$ | $K_g$ | $K_V$ | $K_r$ | $K_i$ |
|----------|---------------------|---------------|-------|-------|-------|-------|-------|
| 59249.29 | NTT+EFOSC2          | 18.3          | -0.03 | -0.04 | 0.00  | 0.00  | -0.00 |
| 59251.57 | 1.0m+Sinistro       | 14.7          | -0.03 | -0.04 | 0.03  | 0.05  | 0.04  |
| 59255.24 | NTT+EFOSC2          | -             | -0.02 | -0.04 | -0.00 | 0.01  | 0.00  |
| 59260.13 | NOT+ALFOSC          | 18.8          | -0.02 | -0.05 | -0.01 | 0.08  | 0.06  |
| 59263.03 | 1.82m+AFOSC         | -             | -0.05 | -0.06 | -0.03 | -0.03 | -0.01 |
| 59276.21 | NTT+EFOSC2          | -             | -0.04 | -0.06 | -0.06 | -0.05 | -0.01 |
| 59286.17 | NTT+EFOSC2          | -             | -0.14 | -0.16 | -0.15 | -0.16 | -0.02 |
| 59288.87 | 1.82m+AFOSC         | -             | -0.12 | -0.13 | -0.08 | -0.10 | -0.07 |
| 59292.40 | 1.0m+Sinistro       | -             | -0.13 | -0.14 | -0.09 | -0.07 | -0.07 |
| 59296.13 | NTT+EFOSC2          | -             | -0.05 | -0.06 | -0.07 | -0.05 | -0.04 |
| 59303.44 | 1.0m+Sinistro       | -             | -0.06 | -0.02 | -0.05 | -0.11 | -0.08 |
| 59312.90 | 1.82m+AFOSC         | 16.7          | -0.13 | -0.12 | -0.07 | -0.12 | 0.52  |
| 59322.86 | NOT+ALFOSC          | 14.4          | -0.19 | -0.17 | -0.07 | 0.07  | -0.03 |
| 59333.45 | 1.0m+Sinistro       | -             | -0.20 | -0.16 | -0.16 | -0.13 | -0.11 |
| 59337.37 | 1.0m+Sinistro       | -             | -0.14 | -0.10 | -0.10 | -0.11 | -0.09 |
| 59338.92 | NOT+ALFOSC          | 14.6          | -0.21 | -0.19 | -0.12 | -0.15 | -0.09 |
| 59347.00 | SEDM                | -             | -0.31 | -0.23 | -0.18 | -0.18 | -0.11 |
| 59348.90 | NOT+ALFOSC          | 18.1          | -0.24 | -0.21 | -0.15 | -0.18 | -0.15 |
| 59359.37 | 1.0m+Sinistro       | 21.9          | -0.19 | -0.05 | -0.04 | -0.12 | -0.13 |
| 59362.88 | NOT+ALFOSC          | 14.9          | -0.27 | -0.23 | -0.15 | -0.13 | -0.08 |
| 59364.00 | Keck+NIRES          | -             | -     | -     | -     | -     | -     |
| 59370.34 | 1.0m+Sinistro       | 15.0          | -0.37 | -0.23 | -0.09 | -0.15 | -0.25 |
| 59375.93 | NOT+ALFOSC          | 16.7          | -0.33 | -0.28 | -0.18 | -0.20 | -0.17 |